The scale-invariant covariance spectrum of brain-wide activity

Zezhen Wang[1,*], Weihao Mai[6,*], Yuming Chai[2,3,*], Kexin Qi[2,3], Hongtai Ren[4], Chen Shen[2,3], Shiwu Zhang[4], Yu Hu[5,6,✉], and Quan Wen[1,2,3,✉]

[1]School of Data Science, University of Science and Technology of China

[2]Division of Life Sciences and Medicine, University of Science and Technology of China, Hefei, China

[3]Hefei National Laboratory for Physical Sciences at the Microscale, Center for Integrative Imaging, University of Science and Technology of China, Hefei, China

[4]Department of Precision Machinery and Precision Instrumentation, University of Science and Technology of China, Hefei, China

[5]Department of Mathematics, The Hong Kong University of Science and Technology, Hong Kong SAR, China

[6]Division of Life Science, The Hong Kong University of Science and Technology, Hong Kong SAR, China

A quantitative characterization of brain-wide activity imposes strong constraints on mechanistic models that link neural circuit connectivity, brain dynamics, and behavior. Here, we analyze whole-brain calcium activity in larval zebrafish captured by fast light-field volumetric imaging during hunting and spontaneous behavior. We found that the brain-wide activity is distributed across many principal component dimensions described by the covariance spectrum. Intriguingly, this spectrum shows an invariance to spatial subsampling. That is, the distribution of eigenvalues of a smaller and randomly sampled cell assembly is statistically similar to that of the entire brain. We propose that this property can be understood in the spirit of multidimensional scaling (MDS): pairwise correlation between neurons can be mapped onto a distance function between two points in a low-dimensional functional space. We numerically and analytically calculated the eigenspectrum in our model and identified three key factors that lead to the experimentally observed scale-invariance: (i) the slow decay of the distance-correlation function, (ii) the higher dimension of the functional space, and (iii) the heterogeneity of neural activity. Our model can quantitatively recapitulate the scale-invariant spectrum in zebrafish data, as well as two-photon and multi-area electrode recordings in mice. Our results provide new insights and interpretations of brain-wide neural activity and offer clues on circuit mechanisms for coordinating global neural activity patterns.

*Equal contribution

Correspondence: *mahy@ust.hk, qwen@ustc.edu.cn*

1 Introduction

Geometrical and statistical analyses of neuronal population activity have shed light on the hidden structures of neural representations and brain dynamics. Dimensionality reduction methods, which seek to identify collective variables or latent variables underlying neural populations, promise to provide a simplified view of high-dimensional neural data (1, 2). Their applications to optical and multi-electrode recordings have begun to reveal important mechanisms by which neural cell assemblies process sensory information (3–5), make decisions (6–8), and generate motor behaviors (9–11). The fundamental reason for thinking of neural computation in terms of a small number of collective variables is the ubiquitous observation of neural correlation, whose structure is shaped by the synaptic connectivity between neurons and the statistics of external stimuli (12, 13). A large body of works has focused on the correlation between neurons (14), which can be measured for a large number of simultaneously recorded neurons within a reasonable amount of time (15). Theoretical analyses on the nature and structure of correlation have implicated its detrimental or beneficial roles in information coding (16–20), as well as its central contribution to synaptic plasticity (21), memory formation, and attention (22–24).

Here, we study the pairwise correlation structure in the brain-wide activity in larval zebrafish described by the covariance matrix, which contains fundamental information about the population activity. The eigenvectors of the covariance matrix correspond to the principal components of Principal Component Analysis (PCA), one of the

widely used dimensionality reduction methods. The *effective dimension* of the subspace spanned by the principal components (PCs) depends on the moments of covariance eigenvalues and has gained much recent interest. On the one hand, many experimental studies that focus on specific brain regions observed low dimensional trajectories of population neural dynamics when animals were engaged in instructed tasks (25, 26). On the other hand, recent analyses of brain-wide activity (27) in freely behaving *C. elegans* (28), *Drosophila* (29), as well as mice (30, 31) revealed that movements- and behavior-related neural activity are distributed across many principal components. Interestingly, several studies discovered that the eigenvalues of the covariance matrix exhibit an approximate power-law distribution in both the full dataset (32, 33) and its coarse-grained version (32), namely iteratively combining maximally correlated neuron pairs. Whereas several theoretical models have been proposed to explain the power-law spectrum (32–35), a general model applicable for brain-wide activity and the conditions for the scale-invariant phenomenon remain elusive.

Using fast light-field microscopy (36), we measured brain-wide calcium activity in larval zebrafish during hunting or spontaneous behavior (Fig. 1A). We found that across 4 animals, the *randomly subsampled* neural covariance matrices appear statistically similar to that of the entire brain (Fig. 1F). The similarity is manifested by plotting the eigenvalues of the subsampled covariance matrices in descending order against their normalized ranks. The eigenvalue curves corresponding to different sizes nearly collapse onto each other except for the largest eigenvalue (Fig. 1G). We verified this observation in datasets recorded by different experimental methods, including light-sheet imaging of larval zebrafish (37), two-photon imaging of mouse visual cortex (31), as well as multi-area Neuropixels recording in mouse (31).

To explain this scale invariance phenomenon, we model the covariance matrix of brain-wide activity by generalizing the Euclidean Random Matrix (ERM) (38): neurons are mapped onto randomly distributed points in a d-dimensional Euclidean space, and pairwise correlation between neurons decays according to their distance in this functional space. Our analytical and numerical calculations point to three key factors that play crucial roles in contributing to the scale invariance of the eigenspectrum: the slow decay of the distance-correlation function, the higher dimension of the functional space, and the heterogeneity of neurons' activity levels. Built upon our theoretical results, we use multidimensional scaling (MDS) and a parameterized distance function to infer the coordinates of each neuron in the functional space, and apply Canonical Correlation Analysis (CCA) to identify a relationship between the anatomical positions of neurons and their locations in the functional space. Taken together, these results bring a new vista of brain-wide activity and its organization, with unexplored consequences on neural computation.

2 Results

2.1 Statistical features of zebrafish brain-wide activity

We simultaneously recorded brain-wide calcium activity at 10 Hz volume rate in head-fixed larval zebrafish using the XLFM microscope (36). The behaviors of the fish, including hunting attempts, were captured by a high-speed infrared camera (50 Hz) (Fig. 1A, B). The hunting behavior, which is composed of stereotyped motor sequences such as eye convergence and J-turn, was triggered by a *live* paramecium whose direction of movement was precisely controlled by a magnetic field (Methods). We recorded spontaneous brain activity and behaviors in the absence of sensory stimuli in one fish as a control. Around 2000 ROIs (1985.8 $\pm$ 762.8, mean $\pm$ SD) with volume 278.9 $\pm$ 381.2 μm^3 (mean $\pm$ SD) were extracted in each fish based on the spatiotemporal activity of each voxel (Methods). These ROIs likely correspond to multiple nearby neurons with highly correlated activity. For the sake of exposition, we refer to the ROIs as "neurons" in the sequel.

Across all four zebrafish in our dataset, the distribution of neural activity covariance C_{ij} (Methods), is broad, positively skewed with a long tail (Fig. 1C, and Fig. S1A-D for all animals and datasets from other studies). The brain-wide activity is also high-dimensional, requiring more than 250 dimensions to explain 50% of the activity variance (Fig. 1D). Consistent with this notion, when the eigenvalues of the covariance matrix are arranged in descending order and plotted against the normalized rank r/N, where $r = 1, \ldots, N$, or the *rank plot*, the curve is approximately a power law, $\lambda \sim (r/N)^{-\alpha}$, for the top 1% to 10% large eigenvalues (Fig. 1G, $\alpha = 0.50 \pm 0.07$, mean$\pm$SD, $R^2 = 97.6 \pm 0.9\%$, mean$\pm$SD, $n = 4$ fish). Most intriguingly, the eigenspectrum curves of smaller, randomly subsampled covariance matrices (i.e., the covariance matrix for N randomly chosen neurons) nearly collapse with each other for a wide range of eigenvalues (except for around the first 1 to 5 eigenvalues, Fig. 1G). We can also directly visualize the similarity of the covariance matrices from randomly sampled neural populations (Fig. 1F) after properly rearranging the neuron indices (Methods).

This observation of *scale invariance* in the covariance matrix is nontrivial and, for example, cannot be reproduced

when we replace its eigenvectors (i.e., the principal components) with a random orthonormal basis while the eigenvalues are kept identical (Fig. 1H, see Methods). Notably, after the eigenvector replacement, the heterogeneity of diagonal entries (i.e., the variance of neural activity) of the covariance matrix becomes much reduced (Fig. 1G,H, gray dots). We will revisit the implication of this observation in section 2.3.

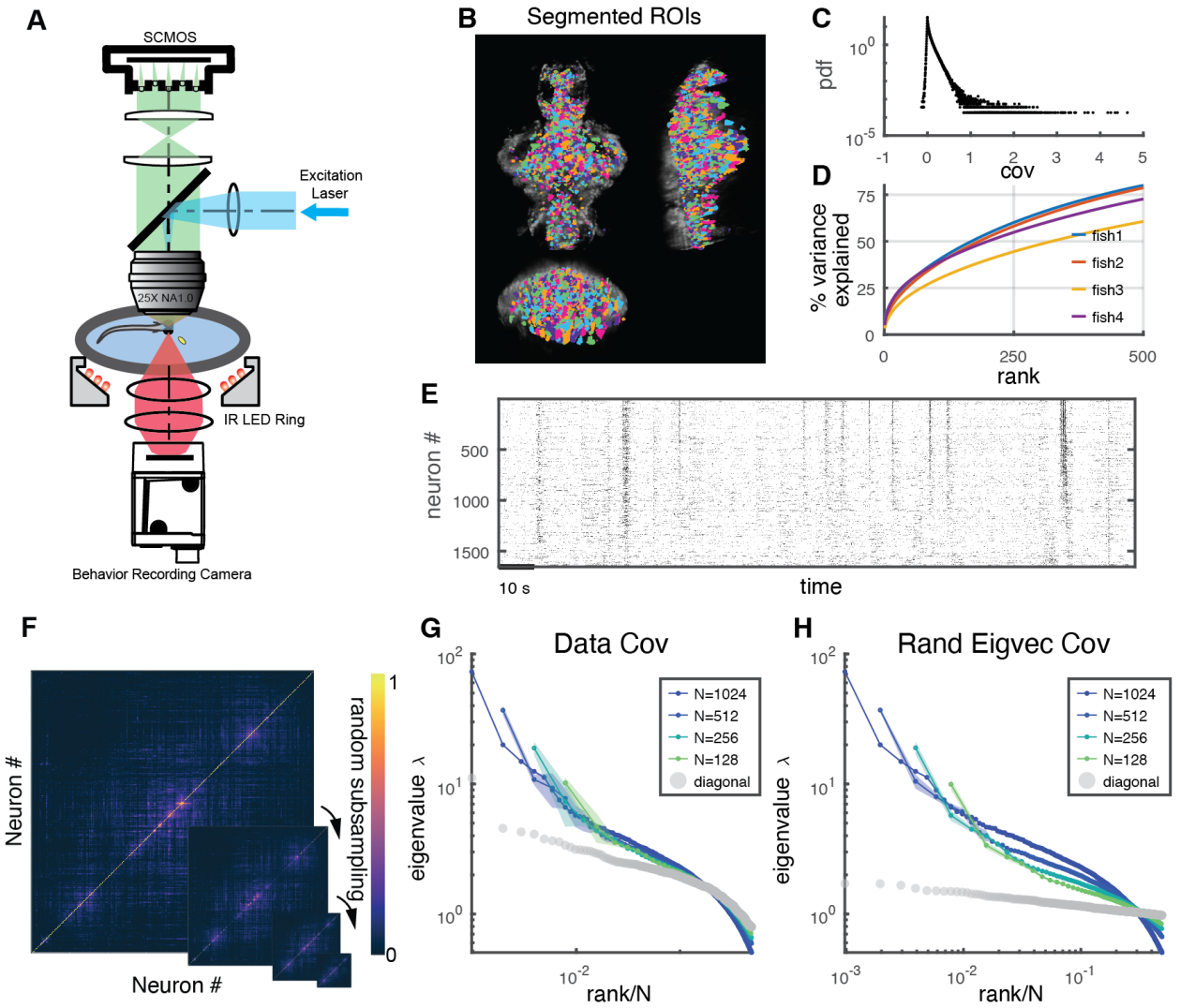

Figure 1. Whole brain imaging of zebrafish neural activity and the phenomenon of its scale-invariant eigenspectrum. A. Fast simultaneous light-field calcium imaging of whole brain neural activity. **B.** Spatial distribution of segmented ROIs (shown in different colors). There are 1347 to 3086 ROIs in each animal. **C.** Distribution of normalized pairwise covariances in an example fish. The mean of diagonal entries of the covariance matrix is normalized to be 1. **D.** Explained variance of the activity data by PCs up to a given rank. Thin lines with different colors represent different fish data (n=4). The dotted green line represents the average across animals. **E.** Example segment of brain-wide neural activity. Black dots represent inferred firing rate. The ROIs are arranged based on their weightings in the first PC. The entire recording for each fish is 16.9±4.5 min (mean±SD). **F.** Iteratively subsampled covariance matrices. The ROI order in each subsampled covariance matrix is re-sorted such that entries near the diagonal exhibit higher covariance. **G. and H.** Subsampled covariance eigenspectra of an example fish data (**G**) and the covariance matrix constructed by substituting with random orthonormal eigenvectors (**H**). N is the number of neurons of the subsampled covariance matrix. The shaded area represents the standard error of the mean (SEM). The rank plot is cutoff after 503 largest eigenvalues, which is the number of Principal Components (PCs) required to explain 90% of the total variance.

2.2 ERM model and two factors contributing to scale invariance

Dimension reduction methods like MDS and tSNE (39, 40), have been widely used to analyze large-scale neural activity data by embedding neurons into a low-dimensional space to reveal functional organizations (37), with nearby neurons showing higher correlations than those that are far away. The Euclidean Random Matrix (ERM

(38)) prescribes a generative model for the covariance matrix in reverse to these ideas of dimensionality reduction. Neurons are assumed to be uniformly randomly distributed in a d-dimensional functional space, $[0, L]^d$. The pairwise correlation between neurons i, j is determined by a *kernel function* $f(\vec{x}_i - \vec{x}_j)$, which is a decreasing function of their distance $\|\vec{x}_i - \vec{x}_j\|$ in this functional space and $f(0) = 1$. The model is also justified by observing a broad and largely positive distribution of covariances in our data (Fig. 1C). To model the covariance matrix, we extend the ERM by introducing heterogeneous variances σ_i^2 of neural activity. σ_i^2 are drawn i.i.d. from a given distribution and are independent with the neuron coordinates $\vec{x}_i$. In sum, the covariance between neuron i and j is given by

$$C_{ij} = \sigma_i \sigma_j f(\vec{x}_i - \vec{x}_j), \quad i, j = 1, 2, \ldots, N. \tag{1}$$

We first explore the ERM with a few forms of $f(\vec{x})$ and find that fast-decaying functions such as the Gaussian pdf $f(\vec{x}) = e^{-\frac{\|\vec{x}\|^2}{2\sigma_x^2}}$ and exponential function $f(\vec{x}) = e^{-\frac{\|\vec{x}\|}{2b}}$ do not lead to eigenspectra similar to those observed in the data and no scale invariance over subsampling (Fig. S3). Therefore, we focus on $f(\vec{x})$ with a slow-decaying, power-law tail $f(\vec{x}) \propto \|x\|^{-\mu}$ for $x \gg 1$, which we find can produce spectra qualitatively similar to data (Fig. 2D,E). Since by definition, $f(0) = 1$, the power law cannot hold near $x = 0$, and modifications are needed to avoid the singularity. In particular, we adopt

$$f(\vec{x}) = \epsilon^{\mu} (\epsilon^2 + \|\vec{x}\|^2)^{-\mu/2}, \tag{2}$$

which approximates a power law $f(\vec{x}) \approx \epsilon^{\mu} \|\vec{x}\|^{-\mu}$ when $\|\vec{x}\| \gg \epsilon$ (Fig. 2B, C). This particular $f(\vec{x})$ is inspired by the Student's t-distribution and we choose it for its analytical tractability in subsequent calculations of the eigenspectrum (see also section 2.4). Note that there is a redundancy between the unit of the functional space (by using a rescaled $\epsilon_\delta \equiv \epsilon/\delta$) and the unit of $f(\vec{x})$ (by using a rescaled $f_\delta(\vec{x}) \equiv f(\vec{x}/\delta)$), so we arbitrarily set ϵ at a fixed value throughout this article.

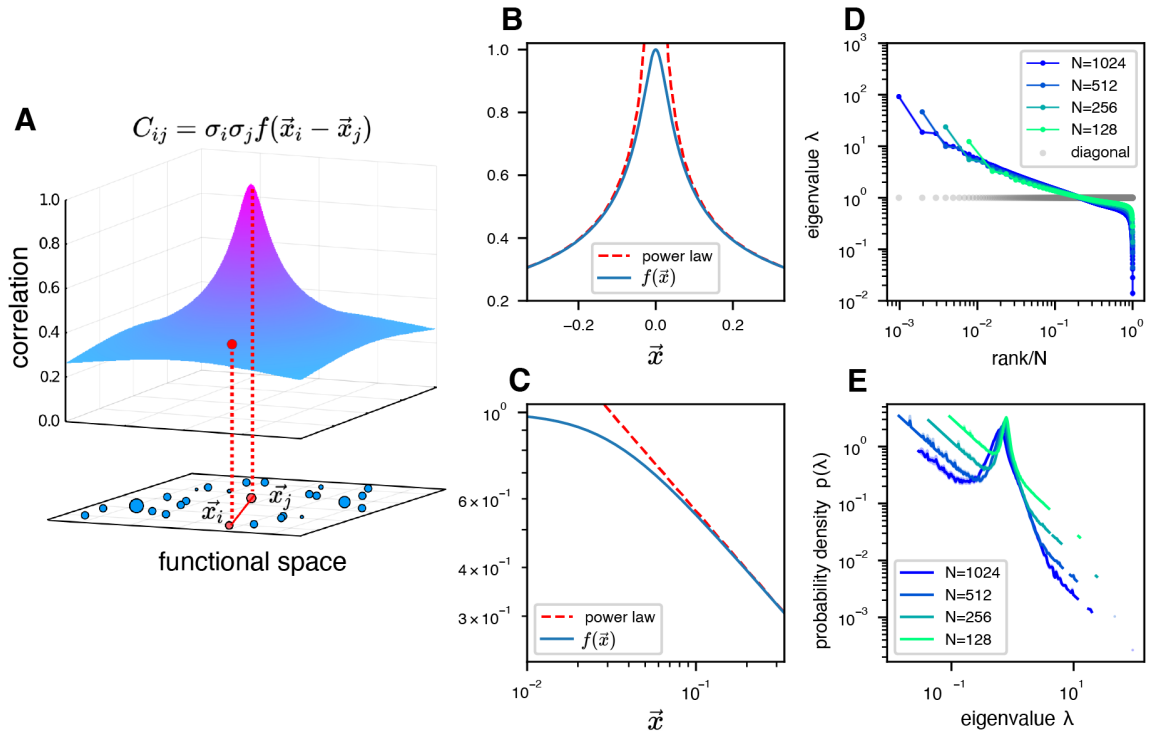

Figure 2. ERM model of covariance and its eigenspectrum. **A.** Schematic diagram of the ERM model. Bottom, scattered blue points represent coordinates of neurons in a $d = 2$ functional space. The bigger the point, the greater its neural activity variance σ_i^2. The functional distance (red line) between two example points (red) determines how strongly the two neurons are correlated according to the kernel function $f(\vec{x})$ (the surface above). The pairwise distance between two points as well as their corresponding sizes together determine the covariance between two neurons. **B.** Visualizing the slow-decaying kernel function $f(\vec{x})$ (blue solid line, Eq. (2)) and its power-law asymptote (red dashed line) along a 1D slice. **C.** Same as **B** except on the log-log scale. **D.** Rank plots of eigenvalues for the ERM correlation matrix (i.e., $\sigma_i^2 = 1$ in Eq. (1) as shown by the rank plot of diagonal entries in gray dots) over random subsampling (colors). The original neuron size is $N = 1024$, $d = 2$, $L = 10$, $\rho = 10.24$ and $f(\vec{x})$ is given by Eq. (2) with $\mu = 0.5$ and $\epsilon = 0.03125$. The curves show the average over 100 ERM simulations, and each ERM uses an identical subsample technique described in (Methods). The shaded area (most are smaller than the marker size) represents SEM. **E.** Same as **C** but for the probability density functions (pdfs).

To understand the properties of the covariance matrix generated as an ERM, we calculate analytically the distribution of eigenvalues, or eigenspectrum, of C (Eq. (1)) in the limit of $N \to \infty$, $L \to \infty$ by generalizing the replica method in (38). A key parameter is the neuron density $\rho := N/L^d$. In the *high-density* regime of $\rho \gg 1$, the probability density function (pdf) of the covariance eigenvalues can be approximated and expressed using the Fourier transform of the kernel function $\tilde{f}(\vec{k})$:

$$p(\lambda) = \frac{1}{\rho \mathrm{E}(\sigma^2)} \int_{\mathbb{R}^d} \frac{d^d \vec{k}}{(2\pi)^d} \delta\left(\frac{\lambda}{\mathrm{E}(\sigma^2)} - \rho \tilde{f}(\vec{k})\right), \tag{3}$$

where $\delta(x)$ is the Dirac delta function and $\mathrm{E}(\sigma^2)$ is the expected value of the variances of neural activity. Without loss of generality, here and below we set $\mathrm{E}(\sigma^2) = 1$ (for simulated and data matrix C, this means multiplying C by a constant such that $\mathrm{Tr}(C)/N = 1$). For the power-law kernel function $f(\vec{x})$ in Eq. (2), it is straightforward to use Eq. (3) to show that for large eigenvalues $\lambda \gg 1$, the eigenspectrum follows a power law (see a derivation in S2):

$$\begin{aligned} p(\lambda) &\sim \rho^{\frac{\mu}{d-\mu}} \lambda^{-\frac{2d-\mu}{d-\mu}}, \\ \text{and equivalently } \lambda &\sim (r/N)^{-1+\frac{\mu}{d}} \rho^{\frac{\mu}{d}}, \end{aligned} \tag{4}$$

where r is the rank of the eigenvalues in descending order. These equations provide intuitive explanations of the scale invariance over spatial subsampling. Note that subsampling in ERM (Eq. (1)) is equivalent to reducing the density ρ. According to Eq. (4), the eigenspectrum becomes ρ-independent or scale-invariant when $\mu/d \to 0$. This predicts two factors contributing to the scale invariance of the eigenspectrum. The first is a small exponent μ in the kernel function $f(\vec{x})$, which means pairwise correlations decay slowly with the functional distance and can be significantly positive across diverse functional modules and throughout the brain. Second, for a given μ, an increased dimension d would improve the scale invariance. The functional space dimension d may be viewed as the neuronal coding space (33); it can also be related to the number of globally projecting latent variables (34) as an alternative interpretation (see also Discussion, S2).

We numerically verify our theoretical predictions of the two contributing factors to the scale invariance by directly comparing the subsampled eigenspectra in finite-size simulated ERMs across different combinations of μ and d (Fig. 3). Based on the discussion ensuing Eq. (3), here we consider the simplified case of $\sigma_i^2 = 1$ (we will revisit this later) in these simulations (Fig. 2D, E and Fig. 3). This also means that entries of C are correlation coefficients. To quantitatively assess the scale invariance, we introduce a collapse index (CI) motivated by Eq. (4). In the log-log scale rank plot, Eq. (4) shows that the spectrum shifts vertically by $\frac{\mu}{d} \log \rho$ for large eigenvalues. Therefore, we define CI as this average displacement (smaller CI means more invariant):

$$\mathrm{CI} := \frac{1}{\log(q_0/q_1)} \int_{\log q_1}^{\log q_0} \left| \frac{\partial \log \lambda(q)}{\partial \log \rho} \right| \mathrm{d} \log q \tag{5}$$

Here q_0 and q_1 are quantiles to select the range of large eigenvalues and their choices are explained in Methods. For simulated ERMs and experimental covariance matrices, CI can be estimated using interpolation and quadrature. Using Eq. (5), Fig. 3 confirms that the scale invariance improves with a slower correlation decay when decreasing μ and when increasing functional dimension d. Note these results further demonstrate that the scale invariance of the covariance is a nontrivial phenomenon: with a large μ and small d, the covariance eigenspectrum can vary with scale significantly (Fig. 3C,D,H).

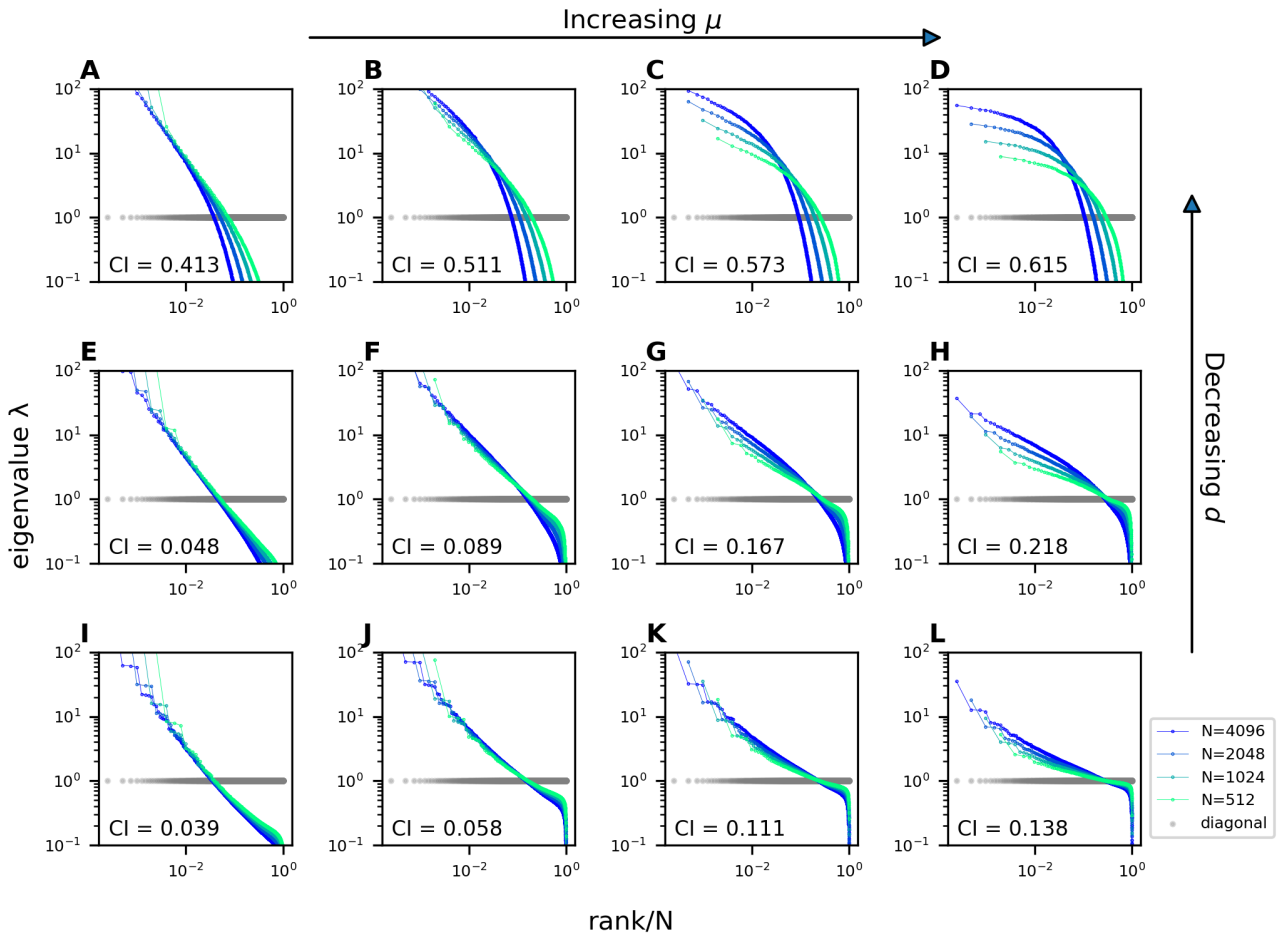

Figure 3. Impact of μ and d on the scale invariance of covariance eigenspectra in ERM. Columns correspond to $\mu = 0.1$, 0.5, 0.9, 1.3, respectively, and rows correspond to $d = 1$, 2, 3, respectively (Eq. (1) and Eq. (2)). Other ERM simulation parameters: $N = 4096$, $\rho = 256$, $L = (N/\rho)^{1/d}$, $\epsilon = 0.03125$ and $\sigma_i^2 = 1$. Each panel is similar to Fig. 2D but shows a single ERM realization. For visualization purposes, the views in some panels are truncated since we use the same range for eigenvalues across all panels.

2.3 Heterogeneous activity levels across neurons enhance scale invariance

So far we have focused on the case of the covariance matrix with $\sigma_i^2 = 1$ in the ERM model (Eq. (1)), which means that C is a correlation matrix. It is then natural to check for any difference between the correlation and covariance matrix spectra. Using the introduced collapsed index (CI), we compare the level of scale invariance of the two spectra in the experimental data. Interestingly, we find that the CI of the covariance matrix is always smaller (i.e., more scale-invariant) across all datasets (Fig. 4A, Fig. S4D, open versus closed squares), suggesting that the heterogeneity of neuronal activity variances σ_i^2 plays an important role in shaping the eigenspectrum.

This finding, however, cannot be explained by the high-density theory Eq. (3), which predicts that the eigenspectrum of the covariance matrix is simply a rescaling of the correlation eigenspectrum by $\mathrm{E}(\sigma_i^2)$, and the heterogeneity of σ_i^2 has no effect when $\rho \gg 1$. This theoretical prediction is confirmed by direct numerical simulations and quantifying the scale invariance using the CI (Fig. S4A). This means that the high-density theory cannot be used to explain the observed change of scale invariance in experimental data shown in Fig. 1G.

Fortunately, we find that the discrepancy between theory and experimental data can be resolved if we consider ERM instead in the *intermediate density* regime $\rho = O(1)$. Here, the resulting CI decreases with $\mathrm{E}(\sigma^4)$ (Fig. 4B), consistent with the observation in the experimental data. A better understanding of this phenomenon requires a more involved calculation of the eigenspectrum based on the Gaussian variational method (38), which specifies the eigenvalue pdf by a set of implicit equations that can be solved numerically (see Methods and S2). The variational theory significantly improves the matching between the ERM simulations at intermediate ρ, where the high-density theory starts to deviate significantly (Fig. 4E,F, Fig. S2). Note that the departure of the leading eigenvalues in these plots is expected since the power-law kernel function we use is not integrable (see Methods for further elaborations).

Moreover, the scale invariance of the spectrum at $\mu/d \to 0$ previously derived using the high-density result Eq. (4) can be extended to the intermediate-density regime by proving the ρ-independence for the variational theory (S2). Finally, using the variational theory, we show that the heterogeneity of population neural activity, quantified by $\mathrm{E}(\sigma^4)$ (recall that we fix $\mathrm{E}(\sigma^2) = 1$, Eq. (3)), indeed improves the collapse of eigenspectra for intermediate ρ (S2). The theory captures the trend of how CI decreases with the heterogeneity of activity variances (Fig. 4B, see Methods for a discussion on the constant bias between theory and ERM simulation).

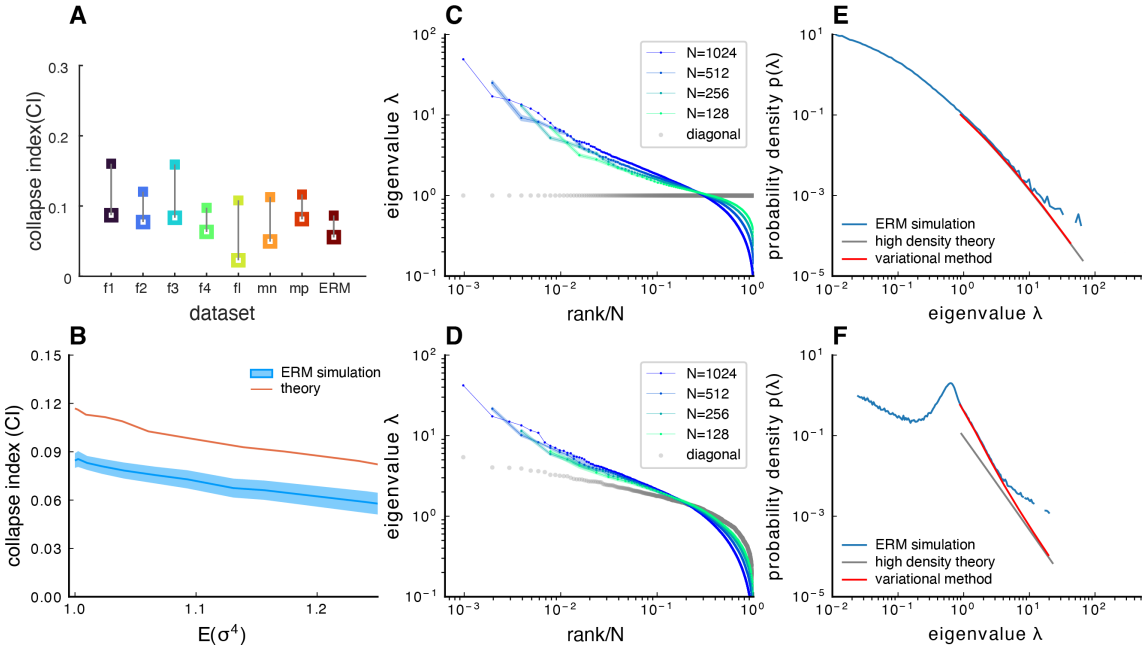

Figure 4. Impact of heterogeneous activity levels. A. The collapse index (CI) of the correlation matrix (filled symbols) is found to be larger than that for the covariance matrix (opened symbols) across different datasets: f1 to f4: four light-field zebrafish data (10 Hz per volume, this paper); fl: light-sheet zebrafish data (2 Hz per volume, (37)); mn: Neuropixels mouse data, 30 Hz downsample to 10 Hz per volume, mp: two-photon mouse data, (3 Hz per volume, (31)). **B.** The CI as a function of the heterogeneity of neural activity levels ($\mathrm{E}(\sigma^4)$). We generate ERM where each neuron's activity variance σ_i^2 is i.i.d sampled from a log-normal distribution with zero mean and a sequence of standard deviation $(0, 0.05, 0.1, \ldots, 0.5)$ in the natural logarithm of the σ_i^2 values. We also normalize $\mathrm{E}(\sigma_i^2) = 1$ (Methods). The solid line is the average across 100 ERM realizations, and the shaded area represents SD. **C.** Subsampled correlation eigenspectra of an example zebrafish data (fish 2). **D.** Same as **C** but for the covariance eigenspectra. **E.** Comparing the pdfs of theoretical spectra (high density and variation method) with finite-size simulations of a high-density ERM. The parameters are $N = 1024$, $\rho = 1024$, $d = 2$, $L = 1$, $\mu = 0.5$, $\epsilon = 0.03125$, $\sigma_i = 1$. **F.** Same as **E** but with $\rho = 10.24$ and $L = 10$. We use 7200 time frames of data across all datasets in **A,C,D**.

2.4 Factors not affecting the scale invariance

Having determined the factors that affect the collapse of the subsampled covariance spectra, we next turn attention to ingredients that have little impact on the scale invariance of the spectrum. First, we find that the shape of the kernel functions $f(\vec{x})$ near $x = 0$ (Fig. S5, table S2) does not affect the distribution of *large eigenvalues* (Fig. 5A). Instead, the distribution of large eigenvalues is determined solely by the tail of $f(x)$ as $x \to \infty$. This further justifies our use of a specific $f(\vec{x})$ (Eq. (2)).

Second, we explore how the spatial distribution of neurons in the functional space, or *coordinate distribution*, affects the collapse of the eigenspectra. Instead of the uniform distribution in a box used in Eq. (1), we generate neurons from a Gaussian distribution or forming clusters (Methods). In all cases of functional coordinate distributions, the large covariance eigenvalues (the top $1\% \to 50\%$ eigenvalues), with the possible exception of leading ones, remain the same (Fig. 5B).

Lastly, we investigate how the geometry of the functional space affects the covariance spectrum. Specifically, we consider two new cases where points are uniformly distributed on the surface of a sphere or a hemisphere embedded in $\mathbb{R}^3$. The eigenspectrum again appears similar to that of the original ERM model where points are uniformly distributed in a 2D box $[0, L]^2$ (Fig. 5C). Taken together, our numerical experiments with modified ERMs suggest that our results on the scale invariance of covariance eigenspectrum in sections 2.2 and 2.3 are robust to various modeling details.

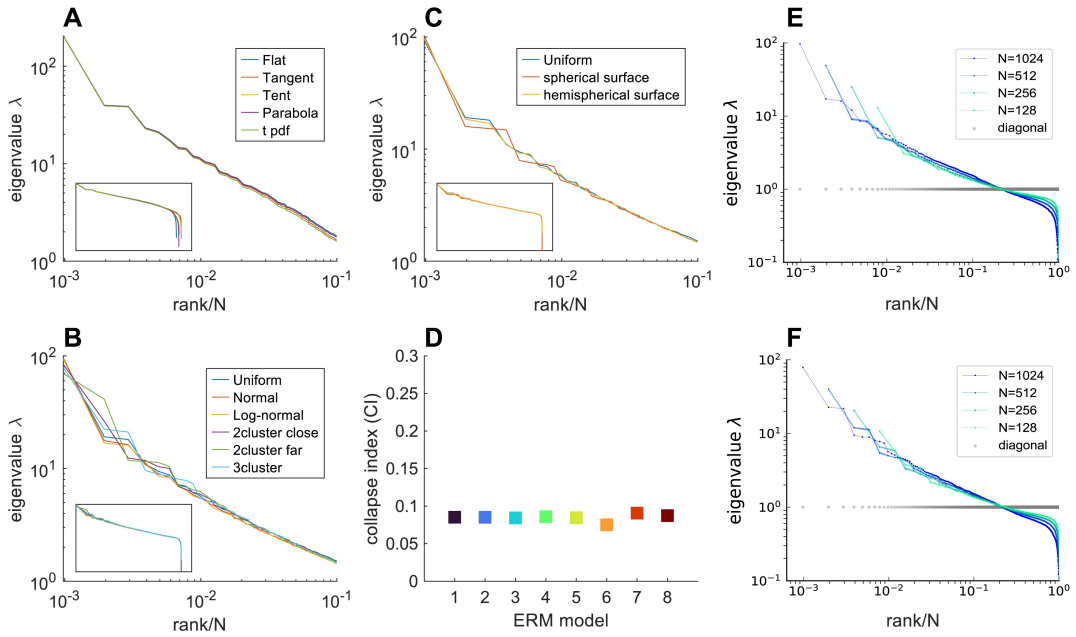

Figure 5. Factors do not affect scale invariance. A. Rank plot of the covariance eigenspectrum for ERMs with different $f(\vec{x})$ (see table S2). **B.** Same as **A** but for different coordinate distributions in the functional space (see text). **C.** Same as **A** but for different geometries of the functional space (see text). **D.** CI of the different ERMs considered in A-C. The y-axis range is identical to Fig. 4A. 1: Uniform distribution, 2: normal distribution, 3: Log-normal distribution, 4: Uniform 2 nearby clusters, 5: Uniform 2 faraway clusters, 6: Uniform 3-cluster, 7: spherical surface in $\mathbb{R}^3$, 8: hemispherical surface in $\mathbb{R}^3$. All ERM models in **B**, **C** are adjusted to have a similar distribution of pairwise correlations (Methods). **E.** Rank plots of eigenvalues for the ERM correlation matrix with Flat $f(\vec{x})$ (table S2) ($f(\vec{x}) = 1$ for values of $x < \epsilon$) and normal coordinate distributions in the functional space. **F.** Rank plots of eigenvalues for the ERM correlation matrix with t-pdf $f(\vec{x})$ (Eq. (2)) and 3-cluster coordinate distributions. ERM simulation parameters: ERM simulation parameters: $\rho = 1024$ and $L = 1$ in **A**. $\rho = 10.24$ and $L = 10$ in **B**,**C**,**E** and **F**. In both cases, the simulations use: $N = 1024$, $\mu = 0.5$, $d = 2$, $\epsilon = 0.03125$ and $\sigma_i^2 = 1$.

2.5 Fitting the ERM model to experimental data

Besides being a conceptually simple model to explain the scale invariance in brain-wide activity, the ERM can also be quantitatively applied to data as a method to analyze and explore the functional structure of neural activity. Our method below consists of two steps, by first fitting the ERM parameters and then use the multidimensional scaling (MDS) (39) to infer the functional coordinate $\vec{x}_i$ of neurons.

For a given dimension d and ϵ (recall ϵ being arbitrarily chosen (section 2.2)), μ of $f(\vec{x})$ (Eq. (2)) and ρ (or equivalently L) (section 2.2) can be fitted by comparing the distribution of pairwise correlations in experimental data and ERM (Methods). We found that an embedding dimension $d \leq 5$ gives an overall better fit than $d > 5$ for the experimental pairwise correlation distribution (Methods). For the sake of simplicity, we use $d = 2$ unless stated otherwise when fitting the kernel function $f(\vec{x})$ and the data covariance matrix. After determining the ERM parameters, we can use $f(\vec{x})$ to translate the experimental pairwise correlations into pairwise distances for all neurons in the functional space. The embedding coordinates $\vec{x}_i$ in the functional space can then be solved through standard optimization in MDS by minimizing the Sammon error (Methods).

With inferred $f(\vec{x})$, embedding coordinates $\vec{x}_i$, as well as data variances $\sigma_i^2 = C_{ii}$, the fitted ERM closely reproduces the experimental covariance matrix (Fig. 6C,D) and its subsampling eigenspectra (Fig. 6A,B); the eigenvalue rank plot has a power-law coefficient $\alpha = 0.45$ that closely matches the experimental $\alpha = 0.50$. Using the embedding coordinates $\vec{x}_i$, we can directly evaluate the similarity between the data $f(\|\vec{x}_i - \vec{x}_j\|)$ and the model $f(\vec{x})$ (Fig. 6E). The matching is close for a wide range of distances, except for small distances and perhaps around the edge of the functional space (see also figures S7 and S8 for plots for all fish datasets). This quantitative similarity with data affirms our choice of considering a power-law $f(\vec{x})$.

MDS also reveals intriguing clustered structures in the functional space (Fig. 6G, also Fig. S9). This makes us wonder about their corresponding brain regions and potential functional roles in the brain-wide circuit. As

a first step, we investigate the relationship between the neural map in the functional space and the anatomical space using the canonical correlation analysis (CCA). In particular, we apply CCA to find a pair of the leading canonical correlation basis vectors $\vec{a}_1$ in the functional space and $\vec{b}_1$ in the anatomical space, respectively (arrows in Fig. 6G,H). These basis vectors satisfy that the projections of neuron coordinates along them, $\{\vec{x}_i \cdot \vec{a}_1\}$ and $\{\vec{y}_i \cdot \vec{b}_1\}$ ($\vec{y}_i$ is the anatomical coordinate), are maximally correlated among all possible choices of $\vec{a}_1$ and $\vec{b}_1$. The comparison with the neuron-shuffled canonical correlation (Fig. 6F) shows that the observed R_{CCA} between embedding coordinates $\vec{x}_i$ and anatomical coordinates $\vec{y}_i$ is highly significant. Interestingly, this R_{CCA} increases with the embedding dimension and saturates when $d > 6$ (Fig. S8I-L). Fig. 6H shows the CCA result for an example fish (fish 4). In this example, $\vec{b}_1$ is approximately parallel to the rostrocaudal axis. When each neuron i is colored by the projection value $\{\vec{y}_i \cdot \vec{b}_1\}$ and displayed in the *functional space* (Fig. 6G), we observe an interesting correspondence between the clustering structures and anatomical coordinate (color). Likewise, we can color each neuron i in the *anatomical space* (Fig. 6H) by the projection value $\{\vec{x}_i \cdot \vec{a}_1\}$, which allows us to observe prominent localizations in brain regions such as the forebrain and the optic tectum. Taken together, our model reveals the phenomenon that functionally clustered neurons are also anatomically segregated (37), and the result is consistent with the literature that the brain-wide circuit in zebrafish is largely organized along the rostrocaudal axis (41).

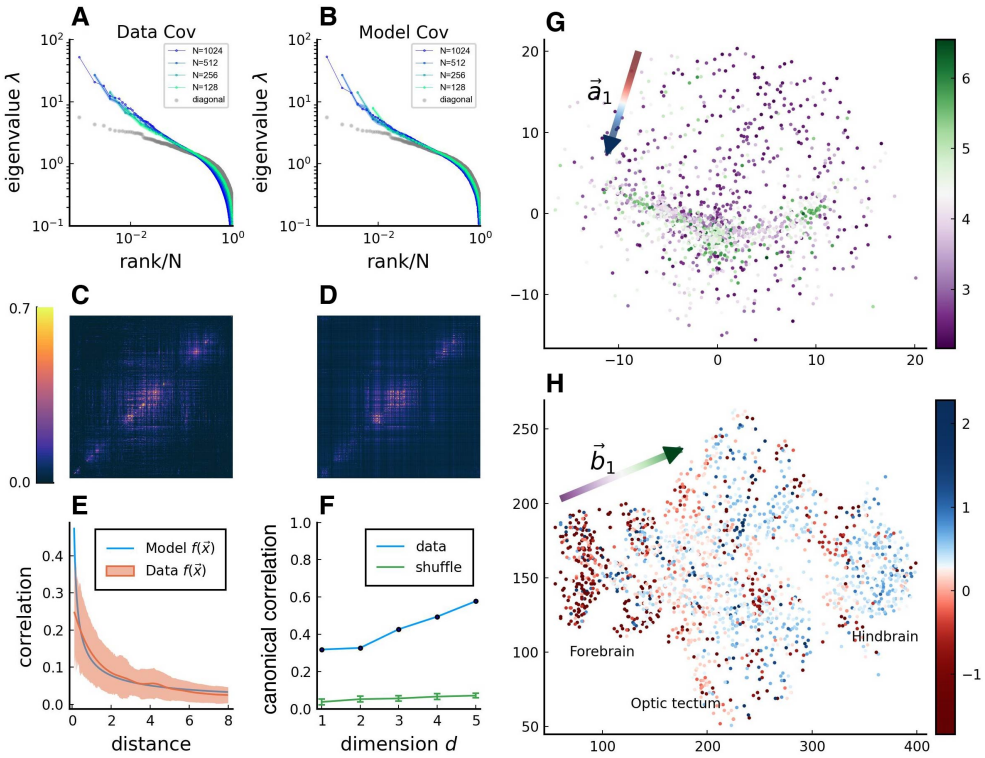

Figure 6. The relationship between functional and anatomical space by ERM fitting to data. A. Subsampled covariance eigenspectra of an example zebrafish data (fish 4). **B.** Subsampled covariance eigenspectra of a fitted ERM model (see text). **C.** Covariance matrix of the example data in **A**. **D.** Covariance matrix of the model in **B**. **E.** Comparison of the power-law kernel function $f(\vec{x})$ in the model in **B** (blue line) and the correlation-distance relationship in the data (red line). The distance is calculated from the inferred coordinates using MDS. The shaded area shows SD. **F.** Top canonical correlation R_{CCA} as a function of embedding dimension d. The blue curve represents the first canonical correlation for the original data, while the green curve is obtained using shuffled coordinates in the functional space. The error bars show SD across 100 trials. **G.** Distribution of neurons in the functional space, where each neuron is color-coded by the projection of its coordinate along the canonical axis $\vec{b}_1$ in anatomical space (see text). **H.** Distribution of neurons in the anatomical space, where each neuron is color-coded by the projection of its coordinate along the canonical axis $\vec{a}_1$ in functional space (see text).

Last but not least, we examine how the hunting behavior (see Fig. 1) would shape the covariance spectrum of brain-wide activity and affect its spatial scale invariance. While our head-fixed animals could not capture the prey, they exhibited characteristic eye convergence (both eyes move inward to focus on a specific object), a behavior commonly associated with hunting in larval zebrafish (42, 43), with a mean duration of 5.95±4.26 sec (mean±SD, n = 60 total number of convergence events across 3 fish under the hunting essay). When removing hunting frames from calculating the covariance matrix, we observe that the scale invariance (i.e., small CI) of the eigenspectra still persists (a similarly small CI like Fig. 4A, Fig. 7). Moreover, the CI for the hunting removed data is comparable with

both the full data and the control case that removes the same number of randomly selected time frames that are not hunting frames. This finding is also consistent with the scale invariance we observed in other datasets where animals were engaged in spontaneous behaviors (Fig. 6A, Fig. S1C-D), suggesting that scale invariance is a general phenomenon in the brain.

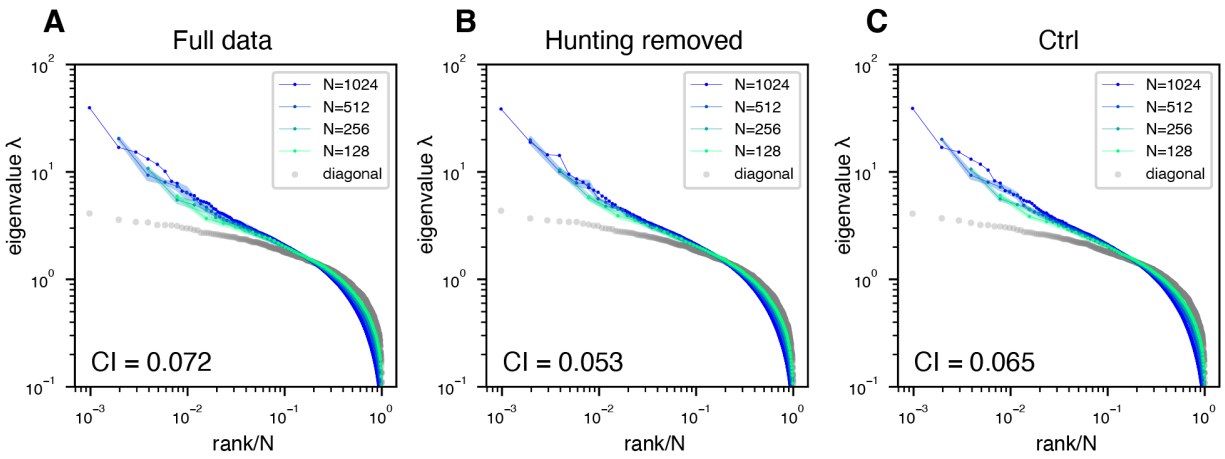

Figure 7. Removing hunting intervals does not obliterate the scale-invariant eigenspectra. Subsampled covariance eigenspectra of the example fish data (fish 2). **A.** Full data: using the entire recording time frames to calculate the covariance matrix. **B.** Hunting removed: time frames corresponding to eye-converged intervals (putative hunting state) are removed in calculating the covariance (Methods). **C.** Ctrl: similarly to **B**, but we randomly remove the same number of time frames that are not those putative hunting frames from the original data.

3 Discussion

In this study, we report that brain-wide neural activity in larval zebrafish is distributed across many dimensions (PCs) with a scale-invariant covariance spectrum. To explain this phenomenon, we use Euclidean Random Matrix (ERM) to model the covariance matrix, where the pairwise correlation is given by a *nonnegative* kernel function $f(\vec{x})$ that monotonically decreases with the distance between neurons in the functional space. This non-negativeness brings a potential issue when applying to experimental data, where, in fact, a small fraction of pairwise correlations/covariances are negative. We have verified that the data covariance matrix spectrum (Fig. S11) remains virtually unchanged when replacing these negative covariances by zero (Fig. S11). This confirms that ERM remains a good model when the neural dynamics is in a regime where pairwise covariances are mostly positive (44) (see also Fig. 1C, Fig. S1A-D).

Our work provides an alternative approach to a recent renormalization approach to characterize the scale-invariance of covariance spectrum (32). Inspired by Kardanoff's block spin transformation (45), Meshulam and colleagues (32) analyzed the collective behavior of cell assembly in mouse hippocampus by iteratively combining maximally correlated neuron pairs and constructing coarse-grained descriptions of neural activity at different scales. When this procedure was used to organize size-dependent covariance matrices, it revealed a scale-invariant power-law eigenspectrum. Our observation, on the other hand, arises from the *random* subsampling of a large neural population. Interestingly, we also observe a similar collapse of eigenspectra in our data using the coarse-graining approach. Despite the technical differences between the two methods, we postulate that there is a fundamental connection between the underlying theories. One possible future direction, for example, would be to carry out the renormalization group procedure in the functional space that is mapped out by multi-dimensional scaling.

One of the key factors we identified contributing to the scale invariance of the covariance spectrum is the slow-decaying, power-law kernel function, $f(\vec{x}) \sim \|\vec{x}\|^{-\mu}$. This kernel function is reminiscent of the spin correlation function at second-order phase transition in equilibrium statistical mechanics (46). Numerous studies in the literature have investigated the critical brain hypothesis, which suggests that when the brain is in a critical state, its information processing capabilities are optimized (44, 47, 48). A noticeable example is the coordinated bursts of activity spanning across cell assemblies, dubbed neuronal avalanches (47) based on an analogy with the sandpile model (49). One, however, must be cautious when making such an analogy. The brain, like many other biological systems, is open and dissipative. As a result, empirical observations of power laws do not necessarily mean that the system

is self-organized into criticality (SOC) (49), see for example (50).

In our ERM model (in the high-density limit), the eigenvalue rank plot obeys a power law $\lambda \sim r^{-\alpha}$, with coefficient $\alpha < 1$. Moreover, a perfect scale-invariance of the subsampled covariance spectra occurs when $\mu/d \to 0$ and the coefficient α approaches 1. We find that experimentally measured eigenspectrum all decayed slower than this critical value with $\alpha < 1$. Interestingly, Stringer and colleagues (33) discovered that in the mouse visual cortex, the neural covariance spectrum in the stimulus space exhibited a power law that decayed faster with $\alpha > 1$; theoretical analysis (33) suggests that $\alpha > 1$ is a mathematical necessity for a smooth and differentiable population code. These two observations are not contradictory since their work (33) was looking at the signal correlation, namely the correlation of neural responses to visual stimuli, by excluding trial-to-trial variability, whereas our covariance is calculated from single-trial activity closer to the noise correlation (51). In addition, the neural activity space representing spontaneous and behavior-related activity and the subspace encoding sensory stimuli may be orthogonal to each other (31), and the corresponding eigenspectra can have very different statistical properties.

A less studied but important factor that improves the collapse of the covariance spectrum is the heterogeneity of neural activity levels (quantified by variance σ_i^2 here). For the sake of simplicity, we assume that neural activity variances $\{\sigma_i^2\}, i = 1, 2, \ldots, N$, are drawn independently in our ERM model (Eq. (1)). To check this assumption, we compare the CI of the original dataset with that of the variance-shuffled data, in which σ_i^2 for different neurons are randomly permuted, while correlations remain the same (this will also modify the covariances $C_{i \neq j}$ according to Eq. (1)). In every light-field fish dataset (f1-f4), 2 out of 3 light-sheet imaging fish datasets, 0 out of 3 Neuropixels datasets, and 2 out of 3 two-photon calcium imaging datasets, the CIs of the original and shuffled data are not significantly different, supporting the independence assumption (Fig. S4C). In the other datasets, however, the CI of the original data is significantly smaller than that of the shuffled data (< 2.5%-quantile), indicating that there are additional fine statistical structures *further improving* the scale invariance of eigenspectrum. How to incorporate these additional covariance structures into the model and characterize their effect on the eigenspectrum is left for future work.

One interesting question, which connects to other lines of research (34, 52), is how the geometry of the functional space/manifold affects the covariance eigenspectrum. With numerical simulations, we find that the geometry of the functional space does not necessarily affect the spectrum and its scale-invariance (Fig. 5). Nevertheless, it is not fully conclusive and welcomes further studies, since we cannot explore all possible topologies of the functional space. Complementary methods, such as the computation of persistent homology (53), may bring new insights into the topological structure of the functional space. Interestingly, one of the cases of a spherical functional space is closely related to a recent model developed by Morrell and colleagues (34), which successfully replicated the coarse-grained scale-invariance phenomenon observed in (32). In the model, neurons are driven by m latent variables with random readout vectors. If we focus on the spatial aspects of neural activity, the model can be approximately viewed as a generalized ERM (54) on a sphere in $\mathbb{R}^{m-1}$ (S2). This connection between the two models means that the dimension of the functional space, which contributes to scale invariance, may also be interpreted as the number of globally projecting latent variables.

Finally, our work illustrated how to fit the ERM to experimental data and infer functional coordinates using MDS. This allows for further quantitative explorations of, for example, the relationship between the functional space and anatomical space in the brain (Fig. 6). An interesting avenue for future research could be to compare how the functional organizations (Fig. 6G) change over different behavior states of the animal (27, 41, 55) or between healthy and diseased subjects.

4 Methods

4.1 Experimental method

The handling and care of zebrafish complied with the guidelines and regulations of the Animal Resources Center at the University of Science and Technology of China (USTC). All larval zebrafish (huc:h2b -GCaMP6f) were raised in E2 embryo medium (containing 7.5 mM NaCl, 0.25 mM KCl, 0.5 mM $MgSO_4$, 0.075 mM KH_2PO_4, 0.025 mM Na_2HPO_4, 0.5 mM $CaCl_2$, and 0.35 mM $NaHCO_3$; also with 0.5 mg/L methylene blue) at 28.5 ℃ and with a 14-h light and 10-h dark cycle.

To induce hunting behavior in larval zebrafish, we fed them with a large amount of paramecia over a period of 4-5 days post-fertilization (dpf). Next, the animals were subjected to a 24-hour starvation period, after which they were transferred to a specialized experimental chamber. The experimental chamber was 20mm in diameter and

Notation	Description
C	covariance matrix, Eq. (1)
C_{ij}	Pairwise covariance between neuron i, j; entries of C
λ	eigenvalue of covariance matrix
$p(\lambda)$	probability density function of covariance eigenvalue, Eq. (3)
r	rank of an eigenvalue in descending order, Eq. (4)
q	fraction of eigenvalues up to λ and $q = r/N$, Eq. (5)
$f(\vec{x}) = f(\|\vec{x}_i - \vec{x}_j\|)$	kernel function or distance-correlation function, Eq. (2)
$\tilde{f}(\vec{k})$	Fourier transform of $f(\vec{x})$
μ	power-law exponent in $f(\vec{x})$, Eq. (2)
ϵ	parameter in $f(\vec{x})$ to smooth the singularity near 0, Eq. (2)
N	number of neurons
L	linear box size of the functional space
ρ	density of neurons in the functional space
d	dimension of the functional space
σ_i^2	variance of neural activity, Eq. (2)
α	power-law coefficient of eigenspectrum in the rank plot, section 2.1
$\vec{x}_i$	neuron i's coordinate in functional space
$\vec{y}_i$	neuron i's coordinate in anatomical space
$\vec{a}_1$	leading canonical correlation basis vector in the functional space, section 2.5
$\vec{b}_1$	leading canonical correlation basis vector in the anatomical space, section 2.5
R_{CCA}	the first canonical correlation, section 2.5

Table 1. Table of notations.

1mm in depth, and the head of each zebrafish was immobilized via the application of 2% low-melting-point agarose. A careful removal of the agarose from the fish's eyes and tail ensured that these body regions remained free to move during hunting behavior. Characteristic behavioral features such as J-turn and eye convergence could thus be observed and analyzed. Subsequently, the zebrafish were transferred into an incubator and stayed overnight. On the 7th dpf, several paramecia were introduced in front of the previously immobilized animals, each of which was monitored by a stereomicroscope. Those displaying binocular convergence were selected for further calcium imaging experiments.

We developed a novel opto-magnetic system (56) that allows (1) precise control of paramecium moving trajectory and (2) brain-wide calcium imaging during zebrafish hunting behavior. To control paramecium movement, we treated these microorganisms with a ferric tetroxide suspension for 30 minutes, and those responsive to magnetic attraction were selected. A magnetic paramecium was placed in front of a selected animal and controlled by a changing

magnetic field generated by Helmholtz coils that were integrated with the imaging system. The real-time position of the paramecium, captured by an infrared camera, was identified by on-line image processing. The positional vector relative to a predetermined target position was calculated. The magnitude and direction of the current in the Helmholtz coils were adjusted accordingly, allowing for precise control of the magnetic field and hence the movement of paramecium. Multiple target positions could be set to drive the paramecium back and forth between multiple locations.

The experimental setup consisted of head-fixed larval zebrafish undergoing two different types of behavior: induced hunting behavior by a moving paramicium in front of a fish (fish 1-3), and spontaneous behavior without any visual stimulus (fish 4). The experiments were performed at ambient temperature (ranging between 23 to 25℃). The zebrafish behavior was monitored by a high-speed infrared camera (Basler acA2000-165umNIR, 0.66x) behind a 4F optical system and was recorded at 50 Hz. Brain-wide calcium imaging was achieved through the XLFM. Light-field images were acquired at 10 Hz, using either customized LabVIEW (National Instruments, US) software or Solis (Oxford Instruments, UK), with the assistance of a high-speed data acquisition card (PCIe-6321, National Instruments, US) to synchronize fluorescence and behavioral imaging.

4.1.1 Behavior analysis. The background of each behavior video was removed using the clone stamp tool in Adobe Photoshop CS6. Individual images were then processed by an adaptive thresholding algorithm, and fish head and yolk were selected manually to determine the head orientation. The entire body centerline, extending from the head to the tail, was divided into 20 segments. The amplitude of a bending segment was defined as the angle between the segment and the head orientation. To distinguish the paramecium from a noisy environment, we subtracted a background image, averaged over a time window of 100 sec, from all frames. The major axis of left or right eye was identified using DeepLabCut (57). The eye orientation was defined as the angle between the rostrocaudal axis and the major axis of an eye; The convergence angle was defined as the angle between the major axes of left and right eyes.

4.1.2 Imaging data acquisition and processing. We employed a fast eXtended Light-Field Microscope (XLFM, with a volume rate of 10 Hz) to record calcium activity across the brain of head-fixed larval zebrafish. Fish were ordered by the dates of experiments. As described previously (36), We adopted the Richardson-Lucy deconvolution method to iteratively reconstruct 3D fluorescence stacks (600 × 600 × 250) from the acquired 2D images (2048 × 2048). This algorithm requires an experimentally measured point spread function (PSF) of the XLFM system.

To perform image registration and segmentation, we first cropped and resized the original image stack to 400 x 308 x 210, which matched the size of a standard zebrafish brain atlas (zbb) (58). This step aimed to reduce substantial memory requirements and computational costs in subsequent operations. Next, we picked a typical volume frame and aligned it with the zbb atlas using a basic 3D affine transformation. This transformed frame was used as a template. We aligned each volume with the template using 3D intensity-based rigid registration (59) and pairwise non-rigid registration (60) in Computational Morphometry Toolkit (CMTK) (61). After voxel registration, We computed the pairwise correlation between nearby voxel intensities and performed watershed algorithm on the correlation map to cluster and segment voxels into consistent ROIs across all volumes. Finally, we adopted the "OASIS" deconvolution method to denoise and infer neural activity from the fluorescence time sequence (62). The deconvolved $\Delta F/F$ of each ROI was used to infer firing rates for subsequent analysis.

4.2 Other experimental datasets

To validate our findings across different recording methods and animal models, we also analyzed three additional datasets. We include a brief description below for completeness. Further details can be found in the respective reference. The first dataset includes whole-brain light-sheet calcium imaging of immobilized larval zebrafish in the presence of visual stimuli as well as in the spontaneous state(37). Each brain volume was scanned through 2.11$\pm$0.21 planes per sec, providing a near-simultaneous readout of neurons' calcium signals. We analyzed fish 8 (69207 neurons $\times$ 7890 frames), 9 (79704 neurons $\times$ 7720 frames) and 11 (101729 neurons $\times$ 8528 frames), which are the first three fish data having more than 7200 frames. For simplicity, we labeled them as l2, l3, and l1(fl). The second dataset consists of Neuropixels recordings from around ten different brain areas in mice during spontaneous behavior (31). The data from the three mice, *Kerbs*, *Robbins*, and *Waksman*, include the firing rate matrices of 1462 neurons $\times$ 39053 frames, 2296 neurons $\times$ 66409 frames, and 2688 neurons $\times$ 74368 frames, respectively. The last dataset comprises two-photon calcium imaging data (2-3 Hz) obtained from the visual cortex of mice during spontaneous behavior. While the dataset includes numerous animals, we focused on the first three animals that exhibited spontaneous behavior:`spont_M150824_MP019_2016-04-05` (11983 neurons $\times$ 21055 frames), `spont_M160825_MP027_2016-12-12` (11624 neurons $\times$ 23259 frames), and

`spont_M160907_MP028_2016-09-26` (9392 neurons $\times$ 10301 frames) (31).

4.3 Covariance matrix and subsampled eigenspectrum

To begin, we multiply each neurons' inferred firing rates (see section 4.1.2) by a constant such that in the resulting activity trace x_i, the mean of x_i *over the nonzero frames* is equal to one (32). Consistent with literature (32), the goal of this step is to remove potential confounding factors in the raw activity traces, such as the heterogeneous expression level of fluorescence protein within neurons, the nonlinear conversion of the electrical signal to calcium concentration, etc. Note that, after this scaling, neurons can still have different activity levels characterized by the variance of x_i, due to differences in activity sparsity (proportion of nonzero frames) and distribution of nonzero x_i values. For consistency, we used the same number of time frames $T = 7200$ when comparing CI across all datasets (Fig. 4, Fig. S4). For other cases (Fig. 1, Fig. 6, Fig. 7, Fig. S1, figures S7 to S11), we analyzed the full length of the data. Next, the covariance matrix was calculated as $C_{ij} = \frac{1}{T-1}\sum_{t=1}^{T}(x_i(t)-\bar{x}_i)(x_j(t)-\bar{x}_j)$, where $\bar{x}_i$ is the mean of x_i over time. Finally, to visualize covariance matrices on a common scale, we multiplied matrix C by a constant such that the average of its diagonal entries equals to one, i.e., $\mathrm{Tr}(C)/N = 1$. This scaling does not alter the distribution of covariance eigenvalues but sets their mean to 1 (see Eq. (3), section 2.2).

We used an iterative procedure to subsample the covariance matrix C (calculated from data or as simulated ERMs). To maintain consistency across datasets, we randomly chose $N_0 = 1024$ neurons from each zebrafish dataset as the initial set of neurons (remain fixed for all analysis). In the first iteration, we randomly select half of the neurons. The covariance matrix for these selected neurons is a $\frac{N}{2} \times \frac{N}{2}$ diagonal block of C. Similarly, the covariance matrix of the un-selected neurons is another diagonal block of the same size. In the next iteration, we similarly create two new subsampled blocks with half number of neurons for each of the blocks we currently have. Repeating this process for n iterations results in 2^n blocks, each containing $N := N_0/2^n$ neurons. At each iteration, the eigenvalues of each block was calculated and averaged after sorting in descending order. Finally, the averaged eigenvalues were plotted against rank/N on a log-log scale. To numerically compute the eigenvalue probability density function in our model, we generated ERM 100 times, each of which was subsampled using the method described above.

To determine the overall power-law coefficient of the eigenspectra, α, throughout the subsampling, we fitted a straight line in the log-log rank plot to the large eigenvalues that combined the original and three-iterations of subsampled covariance matrices (select top 10% eigenvalues for each matrix and excluding the first four largest ones for each matrix). We averaged the estimated α over 10 repeats of the entire subsampling procedure. R^2 of the power-law fit was computed in a similar way.

To visualize the statistical structures of the original and subsampled covariance matrices, the orders of the neurons (i.e., the columns and rows) are determined through the following algorithm. We first constructed a symmetric Toeplitz matrix $\mathcal{T}$, whose entries $\mathcal{T}_{i,j} = t_{i-j}$, and $t_{i-j} \equiv t_{j-i}$. The vector $\vec{t} = [t_0, t_1, \ldots, t_{N-1}]$ is equal to the mean covariance vector of each neuron computed as below. Let $\vec{c_i}$ be a row vector of the data covariance matrix, we identify $\vec{t} = \frac{1}{N}\sum_{i=1}^{N} D(\vec{c_i})$, where $D(\cdot)$ denotes a numerical ordering operator, namely to rearrange the elements in a vector $\vec{c}$ such that $c_0 \geq c_1 \geq \ldots \geq c_{N-1}$. The second step was to find a permutation matrix P such that $\|\mathcal{T} - PCP^T\|_F$ is minimized, where $\| \; \|_F$ denotes the Frobenius norm. This quadratic assignment problem was solved by simulated annealing. Note that after subsampling, the smaller matrix will appear different from the larger one. We need to perform the above re-ordering algorithm for every subsampled matrix such that the matrices of different sizes become similar in Fig. 1F.

The composite covariance matrix with substituted eigenvectors in (Fig. 1H) was created in the following steps. First, we generate a random orthogonal matrix U_r (according to Haar measure) for the new eigenvectors. This is achieved through the QR decomposition $A = U_r R$ of a random matrix A with i.i.d. entries $A_{ij} \sim \mathcal{N}(0, 1/N)$. Next, the composite covariance matrix C_r is defined as $C_r := U_r \Lambda U_r^T$, where Λ is a diagonal matrix containing the eigenvalues of C. Note that since, all the eigenvalues are real and U_r is orthogonal, the resulting C_r is a real and symmetric matrix. By construction, C_r and C have the same eigenvalues, but their *subsampled* eigenspectra can differ.

4.4 ERM model

We consider the eigenvalue distribution or spectrum of the matrix C in the limit of $N \gg 1$ and $L \gg 1$. This spectrum can be analytically calculated in both the high-density ($\rho \gg 1$) and intermediate-density ($\rho = O(1)$) scenarios using the replica method (38). We provide below a sketch of our approach and the detailed derivations can be found in S2.

To calculate the probability density function of the eigenvalues (or eigendensity), we first compute the resolvent or Stieltjes transform $g(z) = -\frac{2}{N}\partial_z \left\langle \ln\, \det(zI - C)^{-1/2} \right\rangle$, $z \in \mathbb{C}$. Here $\langle ... \rangle$ is the average across realizations of C (i.e., random $\vec{x}_i$'s and σ_i^2's). The relationship between the resolvent and the eigendensity is given by the Sokhotski-Plemelj formula:

$$p(\lambda) = -\frac{1}{\pi} \lim_{\eta \to 0^+} \mathbf{Im}\, g(\lambda + i\eta), \tag{6}$$

where $\mathbf{Im}$ means imaginary part.

Here we follow the field-theoretic approach (38), which turns the problem of calculating the resolvent to a calculation of the partition function in statistical physics by using the the replica method. In the limit $N \to \infty$, $L^d \to \infty$, ρ being finite, by performing a leading order expansion of the canonical partition function at large z (S2), we find the resolvent is given by

$$g(z) = \frac{1}{\rho} \int \frac{\mathrm{d}^d k}{(2\pi)^d} \frac{1}{z - \rho E(\sigma^2) \tilde{f}(\vec{k})} \tag{7}$$

the eigendensity for $\rho \gg 1$ (Eq. (3)) can be derived from equations (6) and (7).

In the intermediate density $\rho = O(1)$, an improved approximation can be derived using the Gaussian variational method (38). Unlike the high-density theory where the eigendensity has an explicit expression, here the resolvent $g(z)$ no longer has an explicit expression and is given by the following equation

$$g(z) = \left\langle \frac{1}{z - \sigma^2 \int \mathrm{D}\vec{k}\, \tilde{G}(\vec{k}, z)} \right\rangle_\sigma, \tag{8}$$

where $\langle ... \rangle_\sigma$ computes the expectation value of the term inside the bracket with respect to σ, namely $\langle ... \rangle_\sigma \equiv \int ... p(\sigma) \mathrm{d}\sigma$. Here and below, we denote $\int \mathrm{D}\vec{k} \equiv \int \frac{\mathrm{d}^d \vec{k}}{(2\pi)^d}$. The function $G(\vec{k}, z)$ is determined by a self-consistent equation,

$$\frac{1}{\tilde{f}(\vec{k})} = \frac{1}{\tilde{G}(\vec{k}, z)} + \left\langle \frac{\rho\sigma^2}{z - \sigma^2 \int \mathrm{D}\vec{k}\, \tilde{G}(\vec{k}, z)} \right\rangle_\sigma \tag{9}$$

We can solve $\int \mathrm{D}\vec{k}\, G(\vec{k}, z)$ from Eq. (9) numerically and below is an outline and the details are explained in S2. Let us define the integral $\mathcal{G} \equiv \int \mathrm{D}\vec{k}\, \tilde{G}(\vec{k}, z)$. First, we substitute $z \equiv \lambda + i\eta$ into Eq. (9), and write $\mathcal{G} = \mathbf{Re}\mathcal{G} + i\mathbf{Im}\mathcal{G}$. Eq. (9) can thus be decomposed into its real part and imaginary part, and a set of nonlinear and integral equations, each of which involves both $\mathbf{Re}\mathcal{G}$ and $\mathbf{Im}\mathcal{G}$. We solve these equations in the limit $\eta \to 0$ using a fixed-point iteration alternating between updating $\mathbf{Re}\mathcal{G}$ and $\mathbf{Im}\mathcal{G}$ until convergence.

We find that the variational approximations exhibit an excellent agreement with the numerical simulation for both large and intermediate ρ (for $\rho = 256$ and $\rho = 10.24$, Fig. 4E,F). To further elucidate the connection between the two different methods, we estimate the condition when the result of high-density theory (Eq. (3)) matches that of the variational method (equations (8) and (9)) (S2).

Throughout the paper, we have mainly considered the particular kernel function $f(\vec{x}) = \epsilon^\mu (\epsilon^2 + \|x\|^2)^{-\mu/2}$ (Eq. (2), Fig. 2A, B). This approximate power-law $f(\vec{x})$ has the advantage of having an analytical expression for its Fourier transform, which is crucial for the high-density theory (Eq. (3)),

$$\tilde{f}(\vec{k}) = \frac{2^{\frac{d-\mu+2}{2}} \pi^{\frac{d}{2}} k^{\frac{\mu-d}{2}} \epsilon^{\frac{\mu+d}{2}} K_{(d-\mu)/2}(k\epsilon)}{\Gamma(\mu/2)}, \quad k = \|\vec{k}\| \tag{10}$$

Here $K_\alpha(x)$ is the modified Bessel function of the second kind, and $\Gamma(x)$ is the Gamma function. We calculated the above formulas for $d = 1, 2, 3$ with the assistance of Mathematica and conjectured the case for general dimension d, which we confirmed numerically for $d \leq 10$.

We want to explain two technical points relevant to interpreting our numerical results and choice of $f(\vec{x})$. Unlike the case in the usual ERM, here we allow $f(\vec{x})$ to be non-integrable (over $\mathbb{R}^d$), which is crucial to allow power-law $f(\vec{x})$. The non-integrability violates a condition in classical convergence results of the ERM spectrum (63) as $N \to \infty$. We believe this is exactly the reason for the departure of the first few eigenvalues from our theoretical spectrum (e.g., in Fig. 2). Our hypothesis is also supported by simulations of ERM with integrable $f(\vec{x})$ (Fig. S3),

where the numerical eigenspectrum matches closely with our theoretical one, including the leading eigenvalues. For ERM to be a legitimate model for covariance matrices, we need to ensure the resulting matrix C is positive semidefinite. By Bochner's theorem (64), this is equivalent to the Fourier transform (FT) of kernel function $\tilde{f}(\vec{k})$ to be non-negative for all frequencies. For example, in 1D, a rectangle function $\mathrm{rect}(x) = \begin{cases} 1, & \text{if } |x| \le \frac{1}{2} \\ 0, & \text{otherwise} \end{cases}$ does not meet the condition (its FT is $\mathrm{sinc}(x) = \frac{\sin(x)}{x}$), but a tent function $\mathrm{tent}(x) = \begin{cases} 1-|x|, & \text{if } |x| \le 1 \\ 0, & \text{otherwise} \end{cases}$ does (its FT is $\mathrm{sinc}^2(x)$). For the particular kernel function $f(\vec{x})$ in Eq. (2), this condition can be easily verified using the analytical expressions of its Fourier transform (Eq. (10)). The integral expression for $K_\alpha(x)$, given as $K_\alpha(x) = \int_0^\infty e^{-x\cosh t}\cosh(\alpha t)dt$, shows that $K_\alpha(x)$ is positive for all $x > 0$. Likewise, the Gamma function $\Gamma(x) > 0$. So the Fourier transform of Eq. (2) is positive and the resulting matrix C (of any size and values of $\vec{x}_i$) is guaranteed to be positive definite.

4.5 Collapse index

In the definition of CI (Eq. (5)),

$$\mathrm{CI} := \frac{1}{\log(q_0/q_1)} \int_{\log q_1}^{\log q_0} \left| \frac{\partial \log \lambda(q)}{\partial \log \rho} \right| \mathrm{d}\log q,$$

we set q_1 such that $\lambda(q_1) = 1$, which is the mean of the eigenvalues of a normalized covariance matrix (see section 4.3). The other integration limit q_0 is set to 0.01 such that $\lambda(q_0)$ is the 1% largest eigenvalue.

4.5.1 A calculation of collapse index for experimental datasets/ERM model. To calculate CI for a covariance matrix C of size N_0, we first computed its eigenvalues λ_i^0 and those of the subsampled block C_s of size $N_s = N_0/2$, denoted as λ_i^s (averaged over 20 different random subsamplings). Next, we estimated $\log\lambda(q)$ using the eigenvalues of C_0 and C_s at $q = i/N_s$, $i = 1, 2, \ldots, N_s$. For the subsampled C_s, we simply had $\log\lambda(q = i/N_s) = \log\lambda_i^s$, its i-th largest eigenvalue. For the original C_0, $\log\lambda(q = i/N_s)$ was estimated by a linear interpolation, *on the* $\log\lambda$-$\log q$ *scale*, using the value of $\log\lambda(q)$ at nearest-neighboring $q = i/N_0$'s (which again are simply $\log\lambda_i^0$). Finally, the integral (Eq. (5)) was computed by the trapezoidal rule, discretized at $q = i/N_s$'s, using finite difference $\frac{\partial\log\lambda(q)}{\partial\log\rho} \approx \frac{1}{\log(N_0/N_s)}|\Delta\log\lambda(q)|$, where Δ denotes the difference between the original eigenvalues of C_0 and those of subsampled C_s.

4.5.2 Estimating CI using the variational theory. We first numerically calculated a complementary cdf $q(\lambda)$, the inverse function of $\lambda(q)$ in section 4.5.1, by integrating the probability density function $p(\lambda)$ from λ to a finite $\lambda(q_s)$ rather than to infinity,

$$q(\lambda) = \int_\lambda^\infty p(\lambda)\mathrm{d}\lambda = \int_{\lambda(q_s)}^\infty p(\lambda)\mathrm{d}\lambda + \int_\lambda^{\lambda(q_s)} p(\lambda)\mathrm{d}\lambda = q_s + \int_\lambda^{\lambda(q_s)} p(\lambda)\mathrm{d}\lambda, \tag{11}$$

where $p(\lambda)$ was computed by the variational method equations (8) and (9). The integration limit $\lambda(q_s)$ cannot be directly calculated using the variational theory, we thus use the *high density theory* value $\lambda^h(q_s = 1/N)$ as an approximation. In the intermediate density regime $\rho = O(1)$, since $\lambda^h(q_s = 1/N)$ deviates from the true $\lambda(q_s = 1/N)$, the theoretical CI estimated in this way results in a constant bias in Fig. 4B. Calculating $\lambda(q)$ and $\frac{\partial\log\lambda(q)}{\partial\log\rho}$ directly is difficult, but we can use implicit differentiation

$$\frac{\partial\log\lambda(q,\rho)}{\partial\log\rho} = \frac{\rho}{\lambda(q,\rho)}\frac{\partial\lambda(q,\rho)}{\partial\rho} = -\frac{\rho}{\lambda(q,\rho)}\frac{\frac{\partial q(\rho,\lambda)}{\partial\rho}}{\frac{\partial q(\rho,\lambda)}{\partial\lambda}} \tag{12}$$

and the integral in CI (Eq. (5)) can be rewritten as

$$\int_{\log q_1}^{\log q_0} \left|\frac{\partial\log\lambda(q)}{\partial\log\rho}\right| \mathrm{d}\log q = \int_{q_1}^{q_0} \left| -\frac{\rho}{q\lambda(q)}\frac{\frac{\partial q}{\partial\rho}}{\frac{\partial q}{\partial\lambda}} \right| \mathrm{d}q = \int_{\lambda(q_1)}^{\lambda(q_0)} \left| -\frac{\rho}{q\lambda(q)}\frac{\frac{\partial q}{\partial\rho}}{\frac{\partial q}{\partial\lambda}} \right| \frac{\partial q}{\partial\lambda}\mathrm{d}\lambda = \int_{\lambda(q_0)}^{\lambda(q_1)} \left| \frac{1}{q\lambda(q)}\frac{\partial q}{\partial\log\rho} \right| \mathrm{d}\lambda \tag{13}$$

Since $\frac{\partial q}{\partial\lambda} = -p(\lambda) < 0$, we switch the order of the integration interval in the final expression of Eq. (13).

We next describe how each term inside the integral of Eq. (13) was numerically estimated. First, we calculated $\frac{\partial q}{\partial\log\rho}$ with a similar method described in section 4.5.1. Briefly, we calculated $q_0(\lambda)$ for density $\rho_0 = \frac{N_0}{L^d}$, and $q_s(\lambda)$ for density $\rho_s = \frac{N_s}{L^d}$, and then used the finite difference $\frac{1}{\log(\rho_0/\rho_s)}|\Delta q(\lambda)|$. Second, we calculated $q(\lambda)$ using Eq. (11), where $p(\lambda,\rho)$ was evaluated at $\log\rho = \frac{1}{2}(\log\rho_0 + \log(s\rho_0))$. Here $s = N_s/N_0$, and ρ_0 is the original density

of ERM. Third, $q(\lambda)$ and $\frac{\partial q(\lambda)}{\partial \log \rho}$ were evaluated at $\lambda = \lambda(q_1) + i\frac{\lambda(q_0)-\lambda(q_1)}{k-1}$, where $i = 0, 1, 2, \ldots, k-1$, and we used $k = 20$. Finally, we performed a cubic spline interpolation of the term $\frac{1}{q}\frac{\partial q}{\partial \log \rho}$, and obtained the theoretical CI by an integration of Eq. (13). Fig. 4B shows a comparison between the theoretical CI and that obtained by numerical simulation of ERM (section 4.5.1).

4.6 Extensions of ERM and factors not affecting the scale invariance

In section 2.4 we considered five additional types of spatial density distributions (coordinate distributions) in the functional space and two additional functional space geometries. We examined points distributed according to uniform distribution ($\vec{x} \sim 1/L^d$), normal distribution ($\vec{x} \sim \mathcal{N}(\mu_p, \sigma_p^2\mathbf{I})$), and log-normal distribution ($\log \vec{x} \sim \mathcal{N}(\mu_p, \sigma_p^2\mathbf{I})$). We used the method described in section 4.7.1 to estimate the parameters of coordinate distributions such that they would generate similar pairwise correlation distributions. The relationships between these parameters are described in section 4.7.1. In Fig. 5B, we used the following parameters: $d = 2$; $L = 10$ for uniform distribution; $\mu_p = 0$, $\sigma_p = 2.82$ for normal distribution; $\mu_p = 2$, $\sigma_p = 0.39$ for log-normal distribution.

Second, we introduced multiple clusters of neurons in the functional space, with each cluster uniformly distributed in a box. We considered three arrangements: (1) two closely situated clusters (with a box size of $L = 5\sqrt{2}$, the distance between two cluster centers being $L_c = L$), (2) two distantly situated clusters (with a box size of $L = 5\sqrt{2}$ and inter-cluster distance $L_c = 4L$), and three clusters arrange symmetrically on a equilateral triangle (with a box size of $L = 10/\sqrt{3}$ and inter-cluster distance $L_c = L$).

Finally, we examined the scenario in which points were uniformly distributed on the surface of either a sphere ($4\pi l^2 = L^2$, l being the sphere radius) or a hemisphere ($2\pi l^2 = L^2$) embedded in $\mathbb{R}^3$ (the pairwise distance is that in $\mathbb{R}^3$). It is noteworthy that both cases have the same surface area as the 2D box (section 2.4).

4.7 Fitting ERM to data

4.7.1 Estimating ERM parameters. Our ERM model has 4 parameters: μ, and ϵ dictates the kernel function $f(\vec{x})$; the box size L and the embedding dimension d determine the neuronal density ρ. In the following, we describe an approximate method to estimate these parameters from experimentally measured pairwise correlations $R_{ij} = \frac{C_{ij}}{\sigma_i \sigma_j}$. We proceed by deriving a relationship between the probability density distribution of correlation $h(R)$ and the probability density distribution of pairwise distances $g(u) := g(\|\vec{x}_1 - \vec{x}_2\|)$ in the functional space, from which the parameters of the ERM can be estimated.

Let us consider a distribution of neurons in the functional space with a coordinate distribution $p(\vec{x})$. The pairwise distance density function $g(u)$ is related to the spatial point density by the following formula:

$$g(u) = \int p(\vec{x}_1)p(\vec{x}_2)\delta(\|\vec{x}_1 - \vec{x}_2\| - u)\mathrm{d}\vec{x}_1\mathrm{d}\vec{x}_2 \tag{14}$$

In the case of uniform distribution, $p(\vec{x}_1) = p(\vec{x}_2) = 1/V = 1/L^d$. For other spatial distributions, Eq. (14) cannot be explicitly evaluated. We therefore make a similar approximation by focusing on a small pairwise distance (i.e., large correlation):

$$p(\vec{x}_1) \approx p(\vec{x}_2) \approx p(\frac{\vec{x}_1 + \vec{x}_2}{2}) \tag{15}$$

By a change of variables:

$$\vec{X} = \frac{\vec{x}_1 + \vec{x}_2}{2}, \;\; \vec{u} = \vec{x}_1 - \vec{x}_2,$$

Eq. (14) can be rewritten as

$$g(u) \approx \int p^2(\vec{X})\delta(\|\vec{u}\| - u)\mathrm{d}\vec{X}\mathrm{d}\vec{u} = S_d(u)\int p^2(\vec{X})\mathrm{d}\vec{X} \tag{16}$$

where $S_d(u)$ is the surface area of d-sphere with radius u.

With the approximate power-law kernel function $R = f(u) \approx (\frac{\epsilon}{u})^\mu$, the probability density function of pairwise

correlation $h(R)$ is given by:

$$h(R) = g(u)\left|\frac{\mathrm{d}u}{\mathrm{d}R}\right| = \frac{(2\pi)^{\frac{d}{2}}\epsilon^d}{\Gamma(\frac{d}{2})\mu R^{(\mu+d)/\mu}}\int p^2(\vec{X})\mathrm{d}\vec{X} \tag{17}$$

Taking the logarithm on both sides

$$\log h(R) = \log\left(\epsilon^d\int p^2(\vec{X})\mathrm{d}\vec{X}\right) + \log\frac{(2\pi)^{\frac{d}{2}}}{\Gamma(\frac{d}{2})\mu} - \frac{\mu+d}{\mu}\log R \tag{18}$$

Eq. (18) is the key formula for ERM parameter estimate. In the case of uniform spatial distribution, $\epsilon^d\int p^2(\vec{X})\mathrm{d}\vec{X} = \epsilon^d/V = (\epsilon/L)^d$. For a given d, we therefore can estimate μ and $(\epsilon/L)^d$ separately by fitting $h(R)$ on the log-log scale using linear least square. ϵ and L are a pair of redundant parameters: once ϵ is given, L is also determined. We set $\epsilon = 0.03125$ throughout the article.

Notably, we found that a smaller embedding dimension $d \leq 5$ gave a better fit for the overall pairwise correlation distribution. Below is an empirical explanation. As d grows, to best fit the slope of $\log h(R) - \log R$, μ would also grow. However, for very high dimension d, the y-intercept would become very negative, or equivalently the fitted correlation would become extremely small. This can be verified by examining the leading order $\log R$-independent term in Eq. (18), which can be approximated as $d\log\frac{\epsilon}{L} + \frac{d}{2}\left(\log 2\pi + 1 - \log\frac{d}{2}\right)$. It becomes very negative for large d since $\epsilon \ll L$ by construction. Throughout this article, we use $d = 2$ when fitting experimental data with our ERM model.

The above calculation can be extended to cases when coordinate distribution $p(\vec{x})$ becomes dependent upon other parameters. To estimate the parameters in coordinate distributions that can generate ERMs with similar pairwise correlation distribution (Fig. 5), we fixed the value of the integral $\int p^2(\vec{x})\mathrm{d}\vec{x}$. Consider for example a transformation of uniform coordinate distribution to normal distribution $\mathcal{N}(\mu_p = 0, \sigma_p^2\mathbf{I})$ in $\mathbb{R}^2$. We imposed $\int p^2(\vec{x})\mathrm{d}\vec{x} = 1/(4\pi\sigma_p^2) = 1/L^2$. For log-normal distribution, a similar calculation led to $L\exp(\sigma_p^2/4 - \mu_p) = 2\sqrt{\pi}\sigma_p$. Numerical values for these parameters can be found in section 4.6. Note, however, because of the approximation we used (Eq. (15)), our estimate of the ERM parameters becomes less accurate if the density function $p(\vec{x})$ changes rapidly over a short distance in the functional space. More sophisticated methods, such as grid search, may be needed to tackle such a scenario.

4.7.2 Multidimensional Scaling (MDS). With the estimated ERM parameters (μ in $f(\vec{x})$ and the box size L for given ϵ and d, see section 4.7.1), we performed MDS to infer neuronal coordinates $\vec{x}_i$ in the functional space. First, we computed pairwise correlation $R_{ij} = \frac{C_{ij}}{\sigma_i\sigma_j}$ from data covariances. Next, we calculated the pairwise distance, denoted by u^*_{ij}, by computing the inverse function of $f(\vec{x})$ with respect to the absolute value of R_{ij}, $u^*_{ij} = f^{-1}(|R_{ij}|)$. Finally, we estimated the embedding coordinates $\vec{x}_i$ for each neuron by the SMACOF algorithm (Scaling by MAjorizing a COmplicated Function (65)), which minimizes the Sammon error

$$E = \frac{1}{\sum\limits_{i<j} u^*_{ij}}\sum_{i<j}\frac{(u^*_{ij} - u_{ij})^2}{u^*_{ij}} \tag{19}$$

where $u_{ij} = \|\vec{x}_i - \vec{x}_j\|$ is the pairwise distance in the embedding space calculated above.

To reduce errors at large distances (i.e., small correlations with $R_{ij} < f(L)$, where L is estimated box size), we performed a soft cut-off at a large distance:

$$\begin{aligned} u^*_{ij} &= f^{-1}(|R_{ij}|), & R_{ij} \geq f(L) \\ u^*_{ij} &= L\log(f^{-1}(|R_{ij}|)/L) + L, & R_{ij} < f(L) \end{aligned} \tag{20}$$

During the optimization process, we started at the embedding coordinates estimated by the classical MDS (39), with an initial sum of squares distance error that can be calculated directly, and ended with an error or its gradient smaller than 10^{-4}.

4.8 Canonical-Correlation Analysis (CCA)

Here we briefly explain the CCA method (66) for completeness. The basis vectors $\vec{a}_1$ and $\vec{b}_1$, in the functional and anatomical space, respectively, were found by maximizing the correlation $R_{CCA} = corr(\{\vec{a}_1 \cdot \vec{x}_i\}, \{\vec{b}_1 \cdot \vec{y}_i\})$. Here $\{\vec{x}_i\}$, $\{\vec{y}_i\}$ represent the coordinates in functional and anatomical spaces, respectively. The resulting maximum correlation is R_{CCA} . To check the significance of the canonical correlation, we shuffled the neurons' functional space coordinates $\{\vec{x}_i\}$ across neurons' identity, and re-calculated the canonical correlation with the anatomical coordinates, as shown in Fig. 6F.

4.9 Removing neural activity data during hunting

To identify and remove the time frames corresponding to putative hunting behaviors, the following procedure was used. The hunting interval was defined as from 10 frames (1 sec) preceding the onset of an eye convergence to 10 frames after the offset of this eye convergence. These frames were then excluded from the data before re-calculating the covariance matrix and subsequently the subsampled eigenspectra (Fig. 7B, Fig. S10B,E). As a control to the hunting-frame removal, an equal number of time frames that are not within those hunting intervals were randomly selected and removed and then analyzed (Fig. 7C,Fig. S10C,F). The hunting interval frames and total recording frames for three fish exhibiting hunting behaviors were as follows: fish2 - 565/9774, fish1 - 268/7495, and fish3 - 2734/13904. Fish 4 was not exposed to visual stimuli and therefore was excluded from the analysis.

Code and data availability

The source code and data used to produce all the figures will be available upon publication.

Supplementary information

S1 Supplementary figures. S1 comprises 12 supplementary figures.
S2 Supplementary text. S2 includes further details of theoretical calculations.

Acknowledgment

QW was supported by NSFC-32071008 from National Science Foundation of China and STI2030-Major Projects 2022ZD0211900. YH was supported by ECS-26303921 from Research Grants Council of Hong Kong.

Reference

1. Cunningham, J. P. and Yu, B. M. Dimensionality reduction for large-scale neural recordings. *Nature Neuroscience*, 17(11): 1500–1509, Nov. 2014. doi: 10.1038/nn.3776.
2. Williamson, R. C., Doiron, B., Smith, M. A., and Yu, B. M. Bridging large-scale neuronal recordings and large-scale network models using dimensionality reduction. *Current Opinion in Neurobiology*, 55:40–47, Apr. 2019. doi: 10.1016/j.conb.2018.12.009.
3. Schneidman, E., Berry, M. J., Segev, R., and Bialek, W. Weak pairwise correlations imply strongly correlated network states in a neural population. *Nature*, 440(7087):1007–1012, Apr. 2006. doi: 10.1038/nature04701.
4. Mazor, O. and Laurent, G. Transient Dynamics versus Fixed Points in Odor Representations by Locust Antennal Lobe Projection Neurons. *Neuron*, 48(4):661–673, Nov. 2005. doi: 10.1016/j.neuron.2005.09.032.
5. Si, G., Kanwal, J. K., Hu, Y., Tabone, C. J., Baron, J., Berck, M., Vignoud, G., and Samuel, A. D. Structured Odorant Response Patterns across a Complete Olfactory Receptor Neuron Population. *Neuron*, 101(5):950–962.e7, Mar. 2019. doi: 10.1016/j.neuron.2018.12.030.
6. Briggman, K. L., Abarbanel, H. D. I., and Kristan, W. B. Optical Imaging of Neuronal Populations During Decision-Making. *Science*, 307(5711):896–901, Feb. 2005. doi: 10.1126/science.1103736.
7. Mante, V., Sussillo, D., Shenoy, K. V., and Newsome, W. T. Context-dependent computation by recurrent dynamics in prefrontal cortex. *Nature*, 503(7474):78–84, Nov. 2013. doi: 10.1038/nature12742.
8. Yang, W., Tipparaju, S. L., Chen, G., and Li, N. Thalamus-driven functional populations in frontal cortex support decision-making. *Nature Neuroscience*, 25(10):1339–1352, Oct. 2022. doi: 10.1038/s41593-022-01171-w.
9. Churchland, M. M., Cunningham, J. P., Kaufman, M. T., Foster, J. D., Nuyujukian, P., Ryu, S. I., and Shenoy, K. V. Neural population dynamics during reaching. *Nature*, 487(7405):51–56, July 2012. doi: 10.1038/nature11129.
10. Lindén, H., Petersen, P. C., Vestergaard, M., and Berg, R. W. Movement is governed by rotational neural dynamics in spinal motor networks. *Nature*, 610(7932):526–531, Oct. 2022. doi: 10.1038/s41586-022-05293-w.
11. Urai, A. E., Doiron, B., Leifer, A. M., and Churchland, A. K. Large-scale neural recordings call for new insights to link brain and behavior. *Nature Neuroscience*, 25(1):11–19, Jan. 2022. doi: 10.1038/s41593-021-00980-9. Number: 1 Publisher: Nature Publishing Group.

12. Shadlen, M. N. and Newsome, W. T. The Variable Discharge of Cortical Neurons: Implications for Connectivity, Computation, and Information Coding. *Journal of Neuroscience*, 18(10):3870–3896, May 1998. doi: 10.1523/JNEUROSCI.18-10-03870.1998.
13. Pernice, V., Staude, B., Cardanobile, S., and Rotter, S. How Structure Determines Correlations in Neuronal Networks. *PLoS Computational Biology*, 7(5):e1002059, May 2011. doi: 10.1371/journal.pcbi.1002059.
14. Kohn, A., Coen-Cagli, R., Kanitscheider, I., and Pouget, A. Correlations and Neuronal Population Information. *Annual Review of Neuroscience*, 39(1):237–256, 2016. doi: 10.1146/annurev-neuro-070815-013851. _eprint: https://doi.org/10.1146/annurev-neuro-070815-013851.
15. Cayco-Gajic, N. A., Zylberberg, J., and Shea-Brown, E. Triplet correlations among similarly tuned cells impact population coding. *Frontiers in Computational Neuroscience*, 9, 2015.
16. Yoon, H. and Sompolinsky, H. The Effect of Correlations on the Fisher Information of Population Codes. In *Advances in Neural Information Processing Systems*, volume 11. MIT Press, 1998. URL https://proceedings.neurips.cc/paper/1998/hash/41a60377ba920919939d83326ebee5a1-Abstract.html.
17. Moreno-Bote, R., Beck, J., Kanitscheider, I., Pitkow, X., Latham, P., and Pouget, A. Information-limiting correlations. *Nature Neuroscience*, 17(10):1410–1417, Oct. 2014. doi: 10.1038/nn.3807.
18. Franke, F., Fiscella, M., Sevelev, M., Roska, B., Hierlemann, A., and Azeredo da Silveira, R. Structures of Neural Correlation and How They Favor Coding. *Neuron*, 89(2):409–422, Jan. 2016. doi: 10.1016/j.neuron.2015.12.037.
19. Azeredo da Silveira, R. and Rieke, F. The Geometry of Information Coding in Correlated Neural Populations. *Annual Review of Neuroscience*, 44(1):403–424, 2021. doi: 10.1146/annurev-neuro-120320-082744.
20. Panzeri, S., Moroni, M., Safaai, H., and Harvey, C. D. The structures and functions of correlations in neural population codes. *Nature Reviews Neuroscience*, 23(9):551–567, Sept. 2022. doi: 10.1038/s41583-022-00606-4.
21. Song, S., Miller, K. D., and Abbott, L. F. Competitive Hebbian learning through spike-timing-dependent synaptic plasticity. *Nature Neuroscience*, 3(9):919–926, Sept. 2000. doi: 10.1038/78829.
22. Kanashiro, T., Ocker, G. K., Cohen, M. R., and Doiron, B. Attentional modulation of neuronal variability in circuit models of cortex. *eLife*, 6:e23978, June 2017. doi: 10.7554/eLife.23978.
23. Rosenbaum, R., Smith, M. A., Kohn, A., Rubin, J. E., and Doiron, B. The spatial structure of correlated neuronal variability. *Nature Neuroscience*, 20(1):107–114, Jan. 2017. doi: 10.1038/nn.4433.
24. Huang, C., Ruff, D. A., Pyle, R., Rosenbaum, R., Cohen, M. R., and Doiron, B. Circuit Models of Low-Dimensional Shared Variability in Cortical Networks. *Neuron*, 101(2):337–348.e4, Jan. 2019. doi: 10.1016/j.neuron.2018.11.034.
25. Sadtler, P. T., Quick, K. M., Golub, M. D., Chase, S. M., Ryu, S. I., Tyler-Kabara, E. C., Yu, B. M., and Batista, A. P. Neural constraints on learning. *Nature*, 512(7515):423–426, Aug. 2014. doi: 10.1038/nature13665.
26. Gallego, J. A., Perich, M. G., Naufel, S. N., Ethier, C., Solla, S. A., and Miller, L. E. Cortical population activity within a preserved neural manifold underlies multiple motor behaviors. *Nature Communications*, 9(1):4233, Oct. 2018. doi: 10.1038/s41467-018-06560-z.
27. Kaplan, H. S. and Zimmer, M. Brain-wide representations of ongoing behavior: a universal principle? *Current Opinion in Neurobiology*, 64:60–69, Oct. 2020. doi: 10.1016/j.conb.2020.02.008.
28. Hallinen, K. M., Dempsey, R., Scholz, M., Yu, X., Linder, A., Randi, F., Sharma, A. K., Shaevitz, J. W., and Leifer, A. M. Decoding locomotion from population neural activity in moving C. elegans. *eLife*, 10:e66135, July 2021. doi: 10.7554/eLife.66135.
29. Schaffer, E. S., Mishra, N., Whiteway, M. R., Li, W., Vancura, M. B., Freedman, J., Patel, K. B., Voleti, V., Paninski, L., Hillman, E. M. C., Abbott, L. F., and Axel, R. Flygenvectors: The spatial and temporal structure of neural activity across the fly brain, Sept. 2021. URL https://www.biorxiv.org/content/10.1101/2021.09.25.461804v1.
30. Musall, S., Kaufman, M. T., Juavinett, A. L., Gluf, S., and Churchland, A. K. Single-trial neural dynamics are dominated by richly varied movements. *Nature Neuroscience*, 22(10):1677–1686, Oct. 2019. doi: 10.1038/s41593-019-0502-4.
31. Stringer, C., Pachitariu, M., Steinmetz, N., Reddy, C. B., Carandini, M., and Harris, K. D. Spontaneous behaviors drive multidimensional, brainwide activity. *Science*, 364(6437):eaav7893, Apr. 2019. doi: 10.1126/science.aav7893.
32. Meshulam, L., Gauthier, J. L., Brody, C. D., Tank, D. W., and Bialek, W. Coarse graining, fixed points, and scaling in a large population of neurons. *Physical Review Letters*, 123:178103, 2019. doi: 10.1103/PhysRevLett.123.178103.
33. Stringer, C., Pachitariu, M., Steinmetz, N., Carandini, M., and Harris, K. D. High-dimensional geometry of population responses in visual cortex. *Nature*, 2019. doi: 10.1038/s41586-019-1346-5.
34. Morrell, M. C., Sederberg, A. J., and Nemenman, I. Latent dynamical variables produce signatures of spatiotemporal criticality in large biological systems. *Physical Review Letters*, 126:118302, 2021. doi: 10.1103/PhysRevLett.126.118302.
35. Hu, Y. and Sompolinsky, H. The spectrum of covariance matrices of randomly connected recurrent neuronal networks with linear dynamics. *PLoS Computational Biology*, 18, 7 2022. doi: 10.1371/journal.pcbi.1010327.
36. Cong, L., Wang, Z., Chai, Y., Hang, W., Shang, C., Yang, W., Bai, L., Du, J., Wang, K., and Wen, Q. Rapid whole brain imaging of neural activity in freely behaving larval zebrafish (Danio rerio). *eLife*, 6:e28158, Sept. 2017. doi: 10.7554/eLife.28158.
37. Chen, X., Mu, Y., Hu, Y., Kuan, A. T., Nikitchenko, M., Randlett, O., Chen, A. B., Gavornik, J. P., Sompolinsky, H., Engert, F., and Ahrens, M. B. Brain-wide Organization of Neuronal Activity and Convergent Sensorimotor Transformations in Larval Zebrafish. *Neuron*, 100(4):876–890.e5, Nov. 2018. doi: 10.1016/j.neuron.2018.09.042.
38. Mézard, M., Parisi, G., and Zee, A. Spectra of euclidean random matrices. *Nuclear Physics B*, 559(3):689–701, Oct. 1999. doi: 10.1016/S0550-3213(99)00428-9.
39. Cox, T. and Cox, M. *Multidimensional Scaling*. Chapman and Hall/CRC, 0 edition, Sept. 2000. ISBN 978-0-367-80170-0. doi: 10.1201/9780367801700. URL https://www.taylorfrancis.com/books/9781420036121.
40. Maaten, L. v. d. and Hinton, G. Visualizing Data using t-SNE. *Journal of Machine Learning Research*, 9(86):2579–2605, 2008.
41. Marques, J. C., Li, M., Schaak, D., Robson, D. N., and Li, J. M. Internal state dynamics shape brainwide activity and foraging behaviour. *Nature*, 577(7789):239–243, Jan. 2020. doi: 10.1038/s41586-019-1858-z.
42. Bianco, I. H., Kampff, A. R., and Engert, F. Prey Capture Behavior Evoked by Simple Visual Stimuli in Larval Zebrafish. *Frontiers in Systems Neuroscience*, 5, 2011. doi: 10.3389/fnsys.2011.00101.

43. Semmelhack, J. L., Donovan, J. C., Thiele, T. R., Kuehn, E., Laurell, E., and Baier, H. A dedicated visual pathway for prey detection in larval zebrafish. *eLife*, 3:e04878, Dec. 2014. doi: 10.7554/eLife.04878.
44. Dahmen, D., Grün, S., Diesmann, M., and Helias, M. Second type of criticality in the brain uncovers rich multiple-neuron dynamics. *Proceedings of the National Academy of Sciences*, 116(26):13051–13060, June 2019. doi: 10.1073/pnas.1818972116.
45. Kadanoff, L. P. Scaling laws for ising models near ${T}_{c}$. *Physics Physique Fizika*, 2(6):263–272, June 1966. doi: 10.1103/PhysicsPhysiqueFizika.2.263.
46. Kardar, M. *Statistical Physics of Fields*. Cambridge University Press, Cambridge, 2007. ISBN 978-0-521-87341-3. doi: 10.1017/CBO9780511815881. URL https://www.cambridge.org/core/books/statistical-physics-of-fields/06F49D11030FB3108683F413269DE945.
47. Beggs, J. M. and Plenz, D. Neuronal Avalanches in Neocortical Circuits. *Journal of Neuroscience*, 23(35):11167–11177, Dec. 2003. doi: 10.1523/JNEUROSCI.23-35-11167.2003.
48. Petermann, T., Thiagarajan, T. C., Lebedev, M. A., Nicolelis, M. A. L., Chialvo, D. R., and Plenz, D. Spontaneous cortical activity in awake monkeys composed of neuronal avalanches. *Proceedings of the National Academy of Sciences*, 106(37):15921–15926, Sept. 2009. doi: 10.1073/pnas.0904089106.
49. Bak, P., Tang, C., and Wiesenfeld, K. Self-organized criticality: An explanation of the 1/f noise. *Physical Review Letters*, 59(4):381–384, July 1987. doi: 10.1103/PhysRevLett.59.381.
50. Touboul, J. and Destexhe, A. Power-law statistics and universal scaling in the absence of criticality. *Physical Review E*, 95(1):012413, Jan. 2017. doi: 10.1103/PhysRevE.95.012413.
51. Cohen, M. R. and Kohn, A. Measuring and interpreting neuronal correlations. *Nature Neuroscience*, 14(7):811–819, July 2011. doi: 10.1038/nn.2842.
52. Zhang, H., Rich, P. D., Lee, A. K., and Sharpee, T. O. Hippocampal spatial representations exhibit a hyperbolic geometry that expands with experience. *Nature Neuroscience*, 26(1):131–139, Jan. 2023. doi: 10.1038/s41593-022-01212-4.
53. Giusti, C., Pastalkova, E., Curto, C., and Itskov, V. Clique topology reveals intrinsic geometric structure in neural correlations. *Proceedings of the National Academy of Sciences*, 112(44):13455–13460, Nov. 2015. doi: 10.1073/pnas.1506407112.
54. Karoui, N. E. The spectrum of kernel random matrices. *The Annals of Statistics*, 38(1):1 – 50, 2010. doi: 10.1214/08-AOS648.
55. Muto, A., Lal, P., Ailani, D., Abe, G., Itoh, M., and Kawakami, K. Activation of the hypothalamic feeding centre upon visual prey detection. *Nature Communications*, 8(1):15029, Apr. 2017. doi: 10.1038/ncomms15029.
56. Abbott, J. J., Peyer, K. E., Lagomarsino, M. C., Zhang, L., Dong, L., Kaliakatsos, I. K., and Nelson, B. J. How Should Microrobots Swim? *The International Journal of Robotics Research*, 28(11-12):1434–1447, Nov. 2009. doi: 10.1177/0278364909341658.
57. Mathis, A., Mamidanna, P., Cury, K. M., Abe, T., Murthy, V. N., Mathis, M. W., and Bethge, M. DeepLabCut: markerless pose estimation of user-defined body parts with deep learning. *Nature Neuroscience*, 21(9):1281–1289, Sept. 2018. doi: 10.1038/s41593-018-0209-y.
58. Tabor, K. M., Marquart, G. D., Hurt, C., Smith, T. S., Geoca, A. K., Bhandiwad, A. A., Subedi, A., Sinclair, J. L., Rose, H. M., Polys, N. F., and Burgess, H. A. Brain-wide cellular resolution imaging of Cre transgenic zebrafish lines for functional circuit-mapping. *eLife*, 8:e42687, Feb. 2019. doi: 10.7554/eLife.42687.
59. Studholme, C., Hill, D. L. G., and Hawkes, D. J. Automated three-dimensional registration of magnetic resonance and positron emission tomography brain images by multiresolution optimization of voxel similarity measures. *Medical Physics*, 24(1):25–35, 1997. doi: 10.1118/1.598130.
60. Rueckert, D., Sonoda, L., Hayes, C., Hill, D., Leach, M., and Hawkes, D. Nonrigid registration using free-form deformations: application to breast MR images. *IEEE Transactions on Medical Imaging*, 18(8):712–721, Aug. 1999. doi: 10.1109/42.796284.
61. Rohlfing, T. Computational morphometry toolkit (cmtk). 2011. URL https://www.nitrc.org/projects/cmtk/.
62. Friedrich, J., Zhou, P., and Paninski, L. Fast online deconvolution of calcium imaging data. *PLOS Computational Biology*, 13(3):e1005423, Mar. 2017. doi: 10.1371/journal.pcbi.1005423.
63. Bordenave, C. Eigenvalues of Euclidean random matrices. *Random Structures and Algorithms*, 33(4):515–532, Dec. 2008. doi: 10.1002/rsa.20228.
64. Rudin, W. *Fourier Analysis on Groups*. Wiley, 1 edition, Jan. 1990. ISBN 978-0-470-74481-9 978-1-118-16562-1. doi: 10.1002/9781118165621. URL https://onlinelibrary.wiley.com/doi/book/10.1002/9781118165621.
65. Leeuw, J. d. and Mair, P. Multidimensional Scaling Using Majorization: SMACOF in R. *Journal of Statistical Software*, 31:1–30, Aug. 2009. doi: 10.18637/jss.v031.i03.
66. Knapp, T. R. Canonical correlation analysis: a general parametric significance-testing system. *Psychological Bulletin*, 85(2):410, 1978.
67. Goetschy, A. and Skipetrov, S. Euclidean random matrices and their applications in physics. *arXiv preprint arXiv:1303.2880*, 2013. doi: 10.48550/ARXIV.1303.2880.

Supplementary figures (S1)

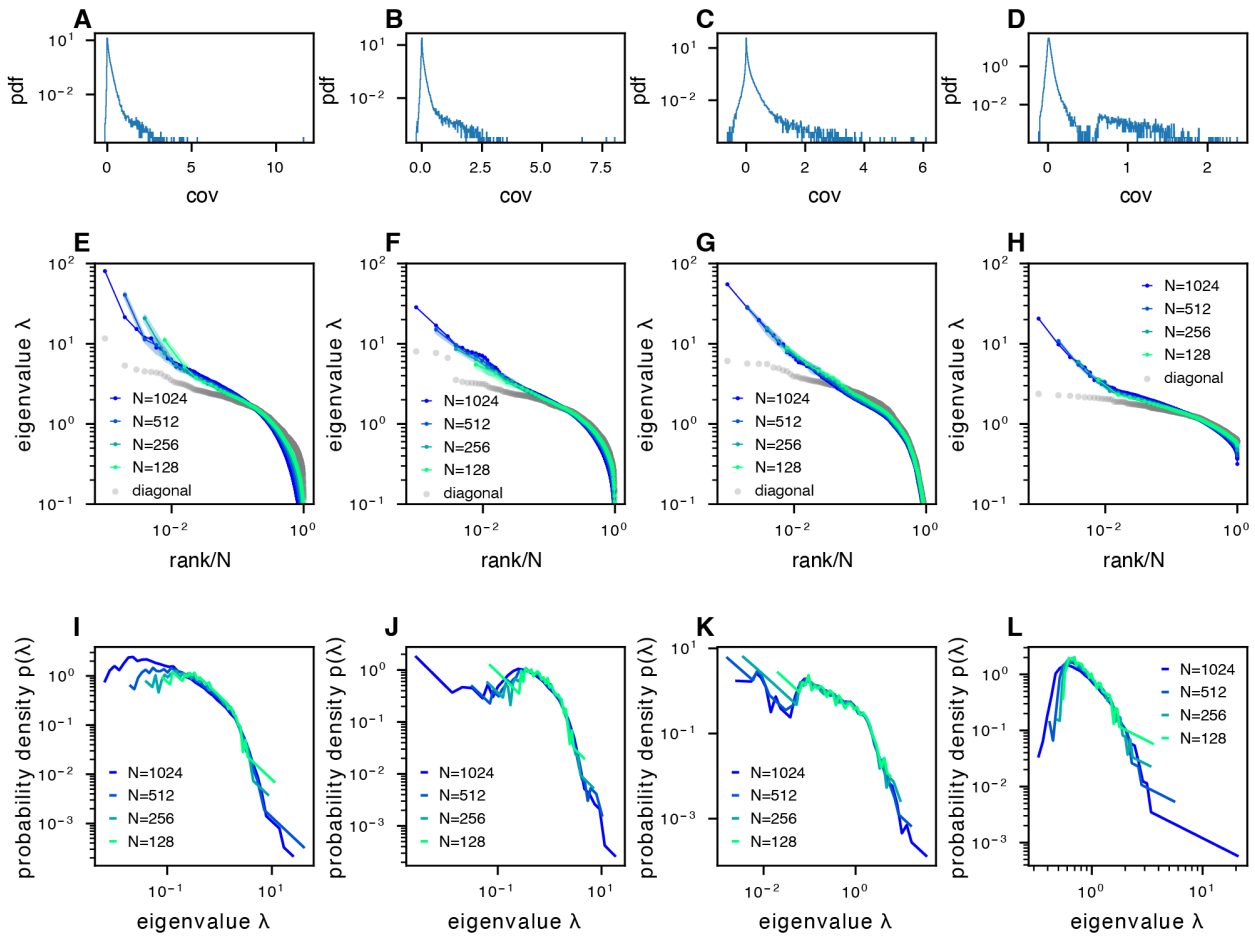

Figure S1. The phenomenon of scale-invariant eigenspectra across different datasets. A-D. Distribution of normalized pairwise covariances, where $\mathrm{E}(\sigma_i^2) = 1$ (Methods). **E-H.** Subsampled covariance eigenspectra of different datasets. **I-L.** Pdfs of subsampled covariance matrix eigenspectra of different datasets. The datasets correspond to the following: column 1: example fish data (fish1) from whole brain light-field imaging; column 2: example fish data from whole brain light sheet imaging; column 3: example mouse data from multi-area Neuropixels recording; column 4: example mouse data from two-photon visual cortex recording.

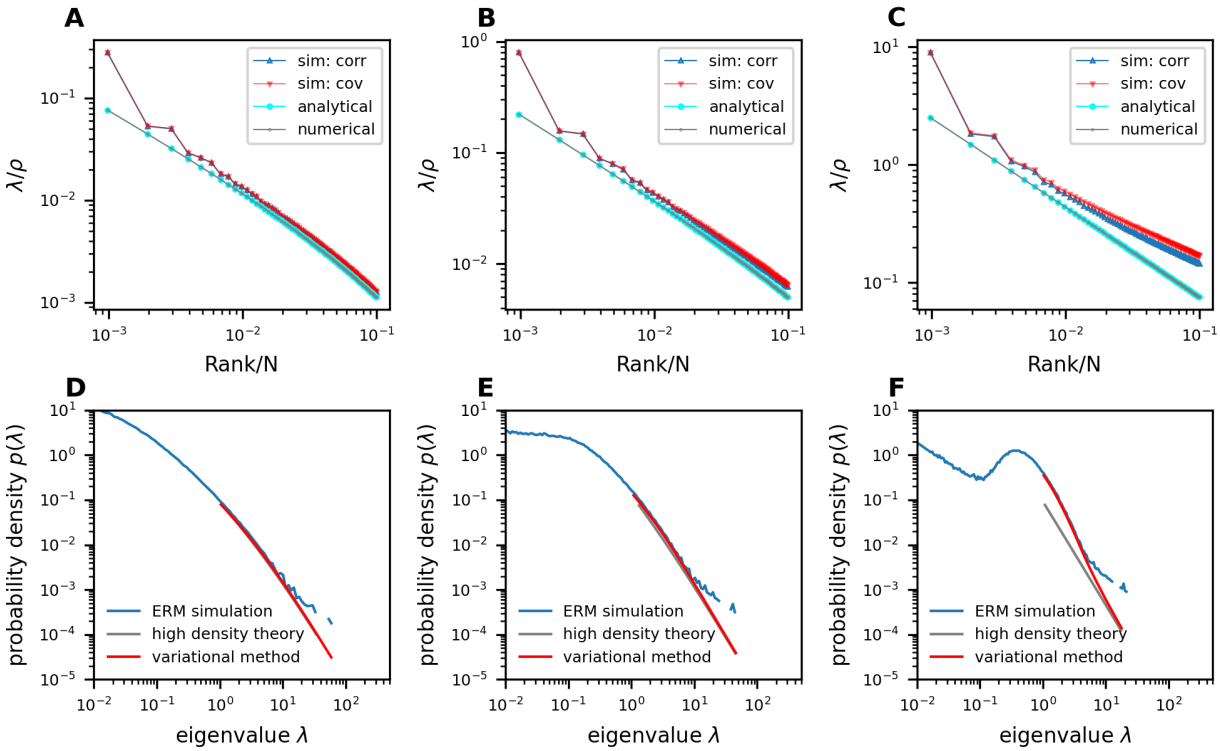

Figure S2. Comparison between ERM simulation and theory. A-C. show rank plots of the normalized eigenspectra (λ/ρ), with the simulations obtained using correlation matrix (sim: corr, $\sigma_i^2 = 1$) and covariance matrix (sim: cov, neuron's activity variance σ_i^2 is i.i.d. sampled from a log-normal distribution with zero mean and a standard deviation of 0.5 in the natural logarithm of the σ_i^2 values; we also normalize $\mathrm{E}(\sigma_i^2) = 1$ (Methods)). The theoretical predictions of normalized eigenvalues λ/ρ are obtained using analytical (cyan) and numerical (gray) calculations of the Fourier transform. The density ρ decreases from panel A to panel C ($\rho = 1024, 256, 10.24$ respectively). **D-F.** show numerical validation of the theoretical spectrum by comparing probability density functions for increasing density of covariance ERM ($\rho = 1024, 256, 10.24$ respectively). Other simulation parameters: $N = 1024$, $d = 2$, $L = (N/\rho)^{1/d}$, $\mu = 0.5$, $\epsilon = 0.03125$. The ERM simulations wereconducted 100 times. The results are presented as the mean ± SEM.

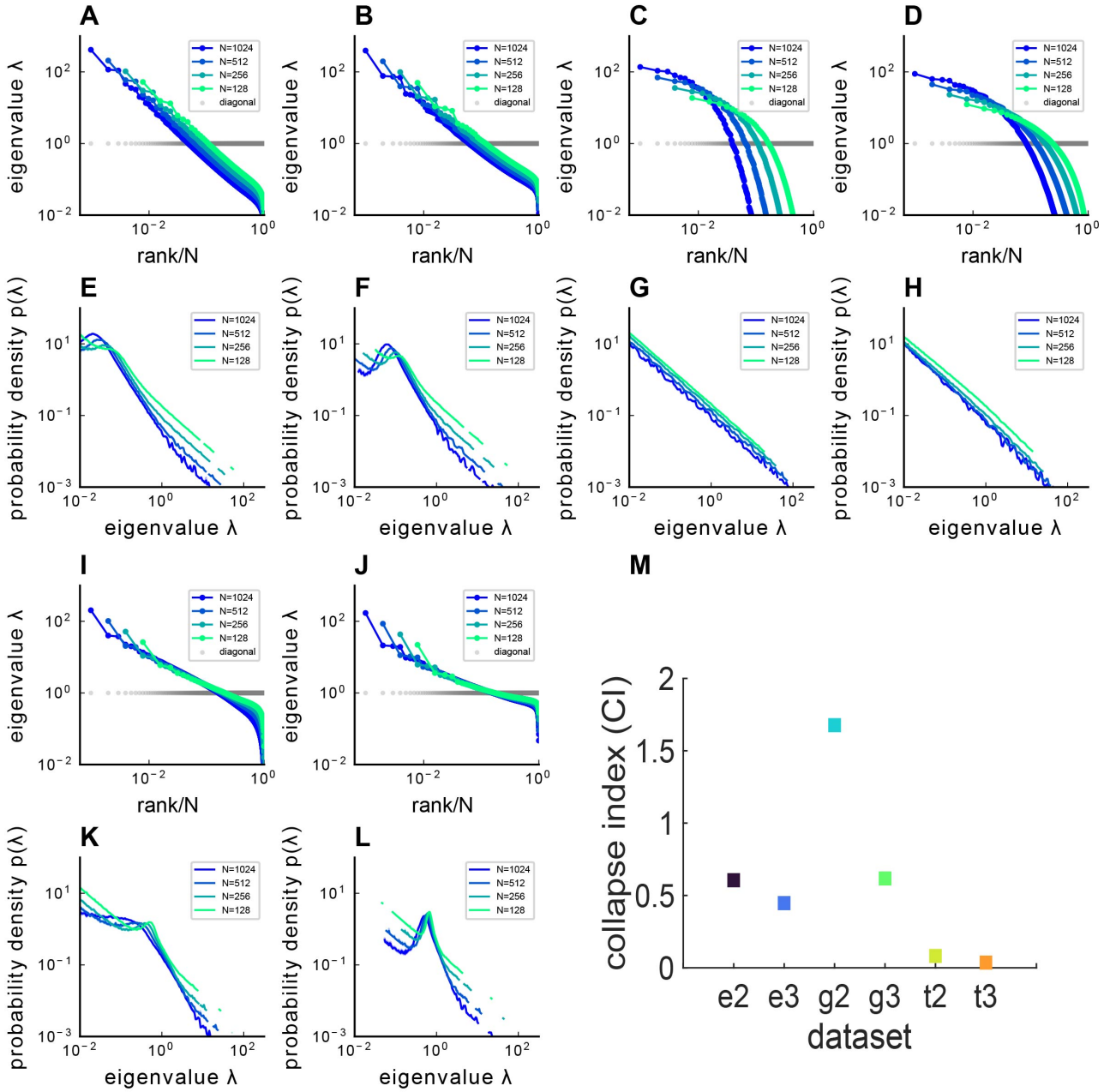

Figure S3. Covariance spectra under other kernel functions $f(\vec{x})$. The figure presents both the subsampled eigenvalue rank plot and the pdf of ERM with different functions $f(\vec{x})$ and varying dimensions d, where panels **A-D,I,J.** display the rank plot and panels **E-H,K,L.** show the pdf of ERM. **A,E.** Exponential function $f(\vec{x}) = e^{-\frac{\|x\|}{2b}}$ and dimension $d = 2$. **B,F.** Exponential function $f(\vec{x}) = e^{-\frac{\|x\|}{2b}}$ and dimension $d = 3$. **C,G.** Gaussian pdf $f(\vec{x}) = e^{-\frac{\|x\|^2}{2\sigma_x^2}}$ and dimension $d = 2$. **D,H.** Gaussian pdf $f(\vec{x}) = e^{-\frac{\|x\|^2}{2\sigma_x^2}}$ and dimension $d = 3$. **I,K.** t pdf Eq. (2) and dimension $d = 2$. **J,L.** t pdf Eq. (2) and dimension $d = 3$. The ERM simulations were conducted 100 times and each ERM uses an identical subsampling technique described in (Methods). The results represent mean ± SEM. **M.** Summary of CI's for different $f(\vec{x})$ and d.

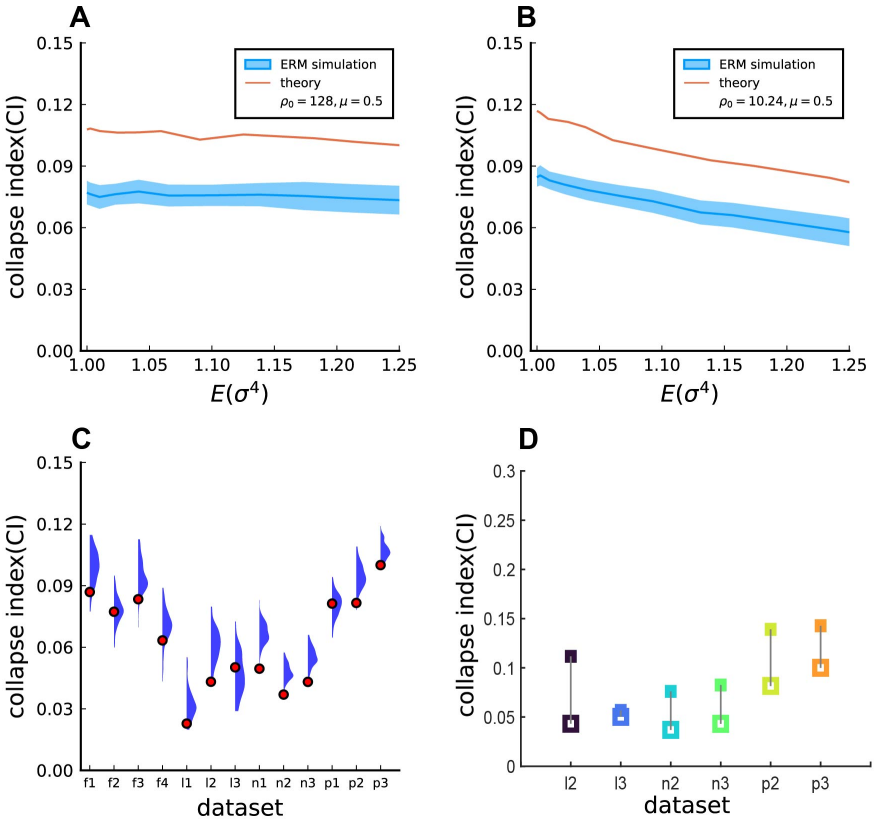

Figure S4. Impact of heterogeneous activity levels on the scale invariance. A. The CI as a function of the heterogeneity of neural activity levels $\mathrm{E}(\sigma_i^4)$. We generate ERM where each neuron's activity variance σ_i^2 is i.i.d. sampled from a log-normal distribution, with the same parameters as in Fig. 4B. The solid blue line is the average across 100 ERM simulations, and the shaded area represents SD. Red line is the result from the Gaussian variational theory. $\rho_0 = 128$. **B.** Same as A, but with a smaller $\rho_0 = 10.24$. Other parameters: $\mu = 0.5$, $d = 2$, $N = 1024$, $L = (N/\rho)^{1/d}$, $\epsilon = 0.03125$. **C.** Comparison of the collapse index between experimental data and shuffled data, red: collapse index of experimental data, blue: collapse index distribution of shuffled data. datasets: f1 to f4: four light-field zebrafish data (10 Hz per volume, Methods); l1 (fl) to l3: light-sheet zebrafish data (2 Hz per volume); n1 (mn) to n3: Neuropixels mouse data, 30 Hz downsample to 10 Hz per volume, p1 (mp) to p3: two-photon mouse data, (3 Hz per volume). **D.** The collapse index (CI) of the correlation matrix (filled symbols) is larger than that of the covariance matrix (opened symbols) across different datasets excluding those shown in Fig. 4. We use 7200 time frames data across all datasets.

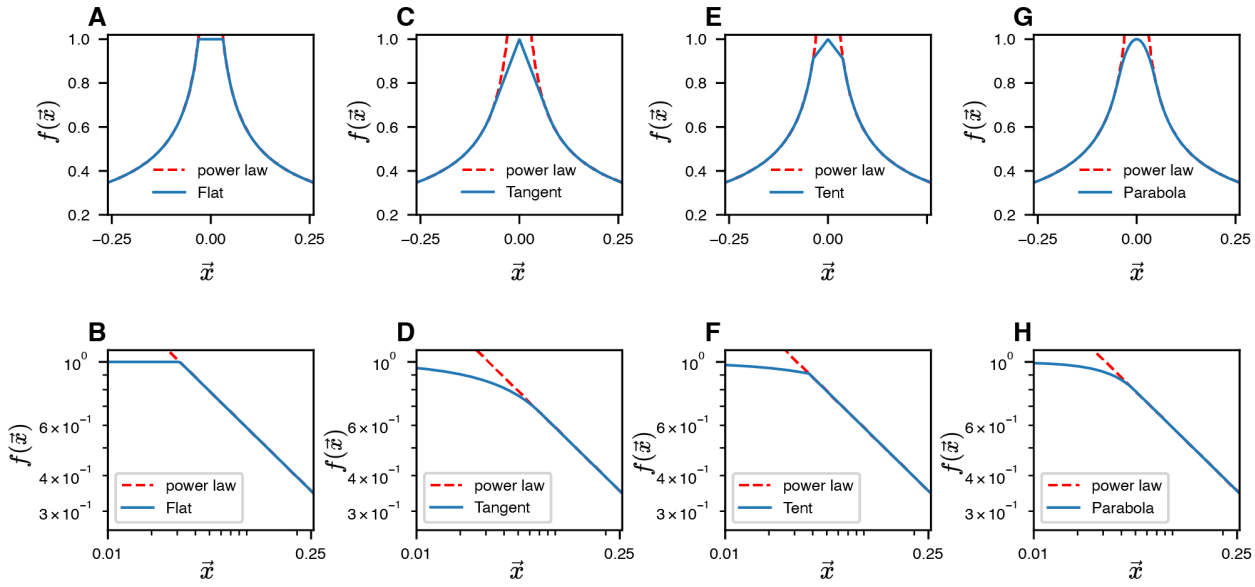

Figure S5. Modifications $f(\vec{x})$ near $x = 0$ other than the t pdf (Eq. (2)) The first row illustrates the slow-decaying kernel function $f(\vec{x})$ (blue solid line) and its power-law asymptote (red dashed line) along a 1D slice at various $f(\vec{x})$. The second row is similar to **A**, but on the log-log scale.

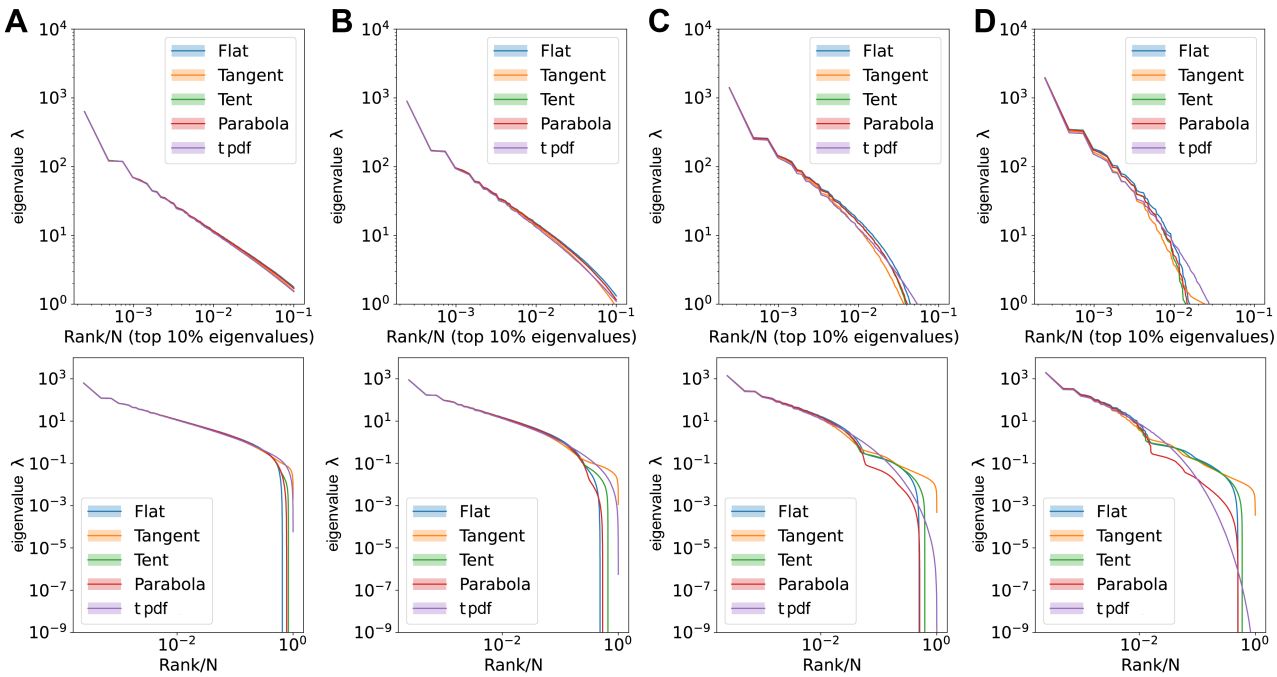

Figure S6. Comparisons of large eigenvalues across different smoothing interval sizes, ϵ. Rank plot (first row) and pdf (second row) of the covariance eigenspectrum for ERMs with different $f(\vec{x})$ (see table S2). **A.** $\epsilon = 0.06$. **B.** $\epsilon = 0.12$. **C.** $\epsilon = 0.3$. **D.** $\epsilon = 0.6$. Other ERM simulation parameters: $N = 4096$, $\rho = 100$, $\mu = 0.5$, $d = 2$, $L = 6.4$, $\sigma_i^2 = 1$.

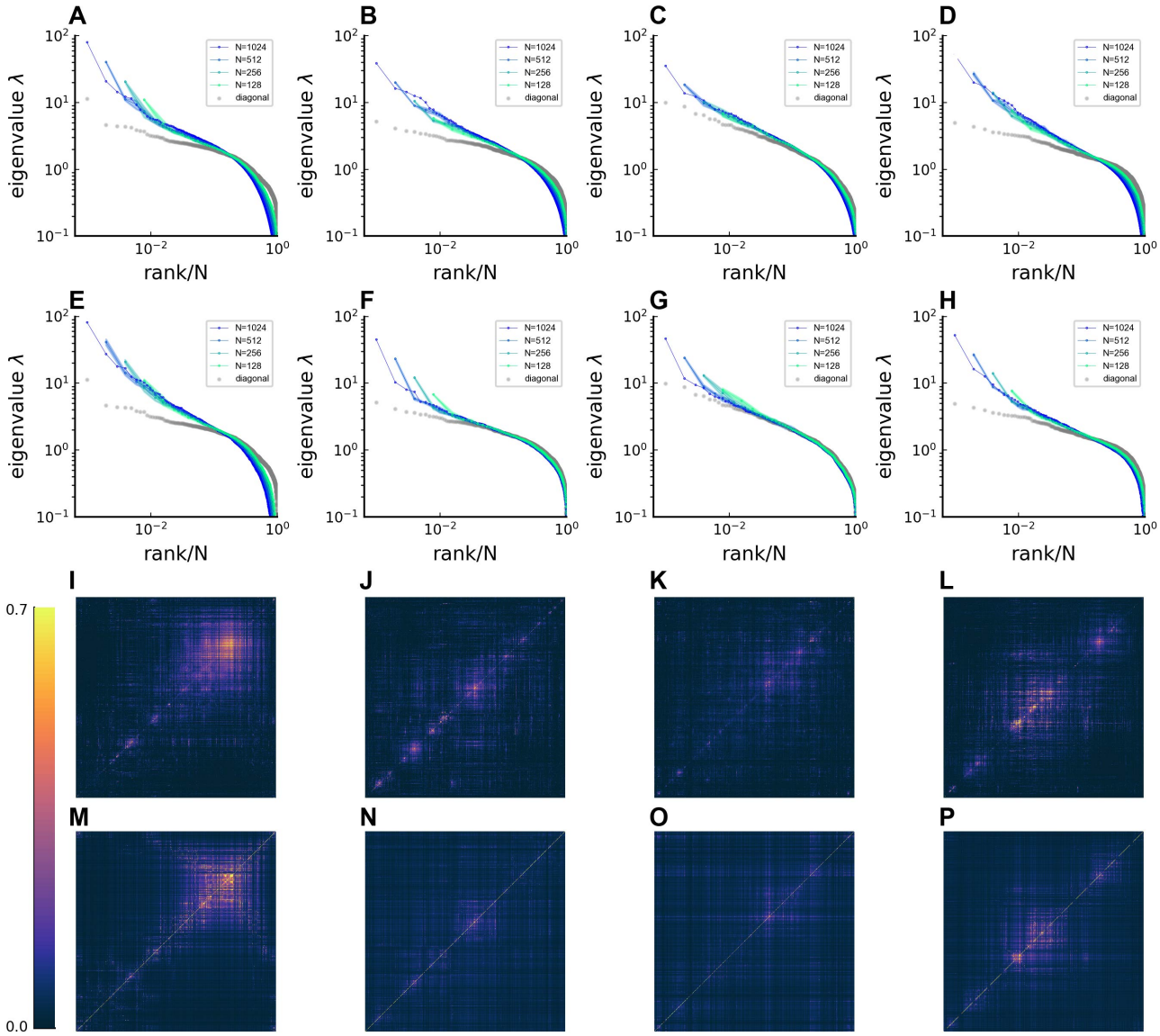

Figure S7. Fitting ERM to all four zebrafish data from our experiments (part1). Comparison of subsampled eigenspectrum and covariance matrix between fish data and fitted model. The columns correspond to four light-field zebrafish data: fish 1 to fish 4 (with fish 4 has been shown in Fig. 6). **A-D.** Subsampled covariance eigenspectra of different fish data. **E-H.** Subsampled covariance eigenspectra of model fitted from different fish data. **I-L.** Covariance matrix of different fish data. **M-P.** Covariance matrix of model inferred from different fish data.

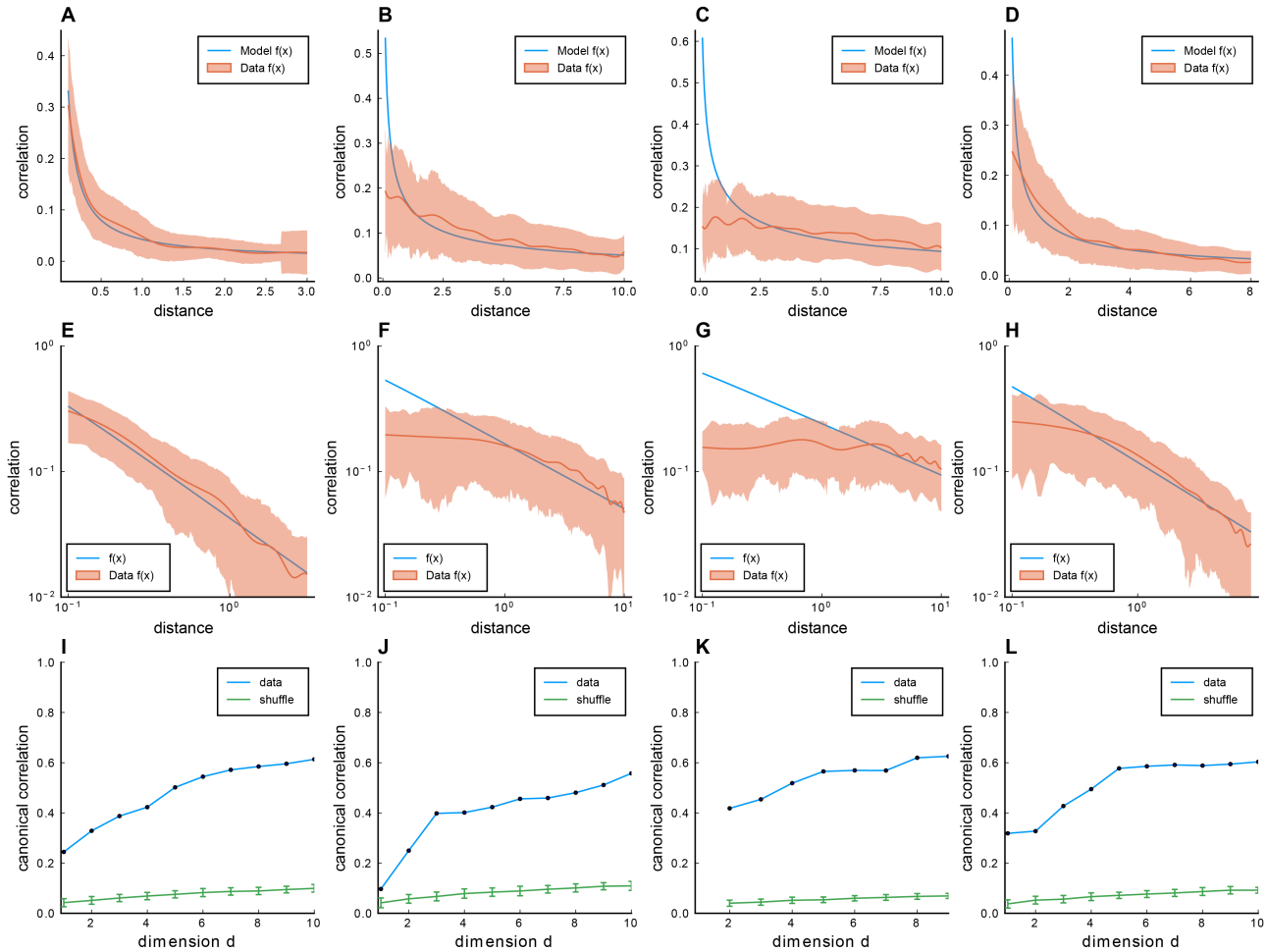

Figure S8. Fitting ERM to all four zebrafish data from our experiments (part2). Similar to Fig. S7, columns correspond to four light-field zebrafish data: fish 1 to fish 4. **A-D**: Comparison of the power-law kernel function $f(\vec{x})$ in the model (blue line) and the correlation-distance relationship in the data (red line). The distance is calculated from the inferred coordinates using MDS. The shaded area represents SD. **E-H**: Same as A-D but on the log-log scale. **I-L**: CCA correlation between the first CCA variables with different embedding dimensions in the functional space. Blue indicates CCA correlation of example fish data, green shows CCA correlation of example fish data with shuffled functional coordinates, and error bar represents SD.

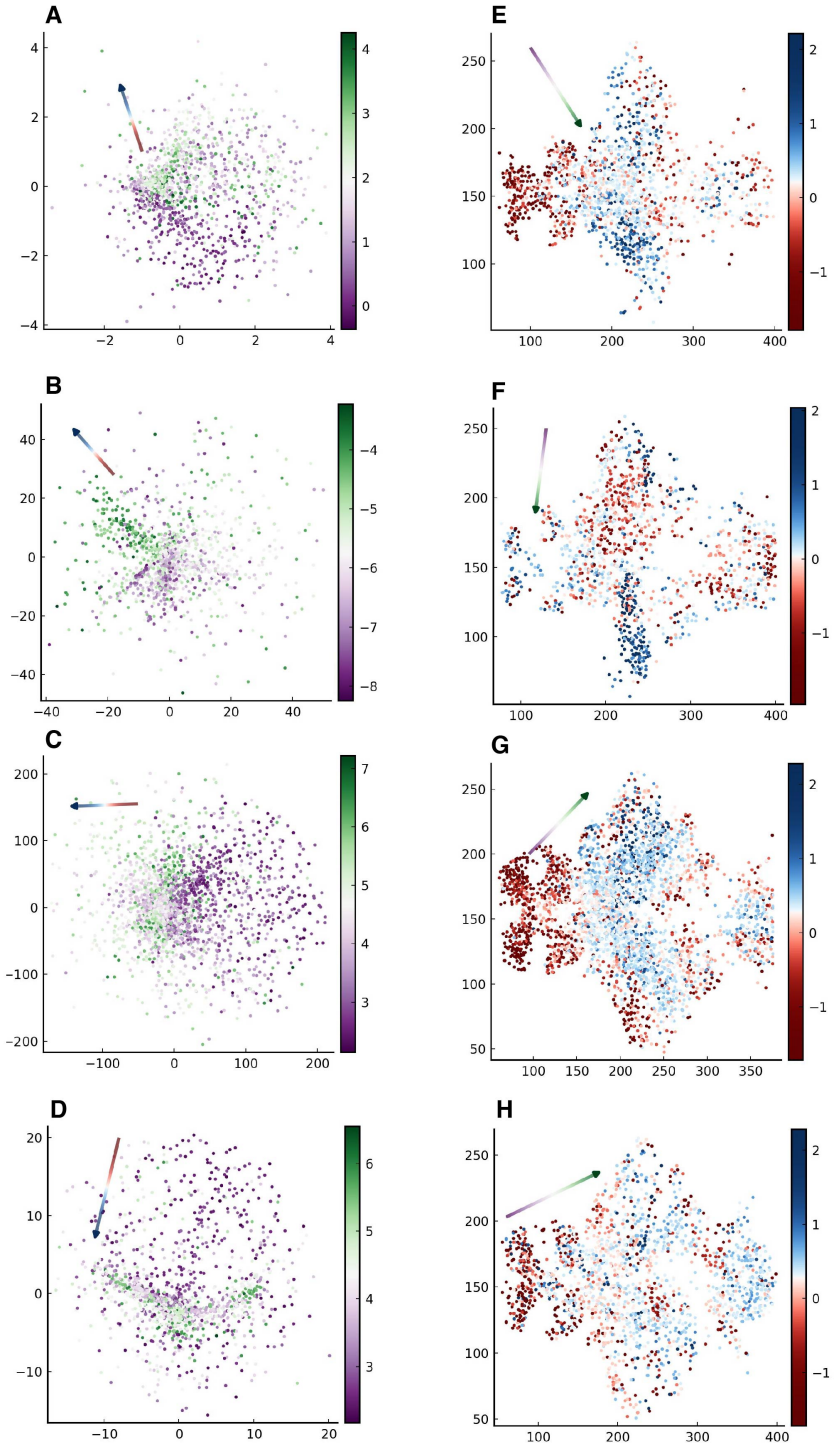

Figure S9. Relationship between the functional space and anatomical space for each zebrafish dataset from our experiments. Columns correspond to four light-field zebrafish data: fish 1 to fish 4. **A-D.** Distribution of neurons in the functional space, where each neuron is color-coded by the projection of its coordinate along the canonical axis $\vec{b}_1$ in anatomical space (see text in section 2.5). Arrow: the first CCA direction $\vec{a}_1$ in functional space. **E-H.** Distribution of neurons in the anatomical space, where each neuron is color-coded by the projection of its coordinate along the canonical axis $\vec{a}_1$ in functional space (see text in section 2.5). Arrow: the first CCA direction $\vec{b}_1$ in anatomical space.

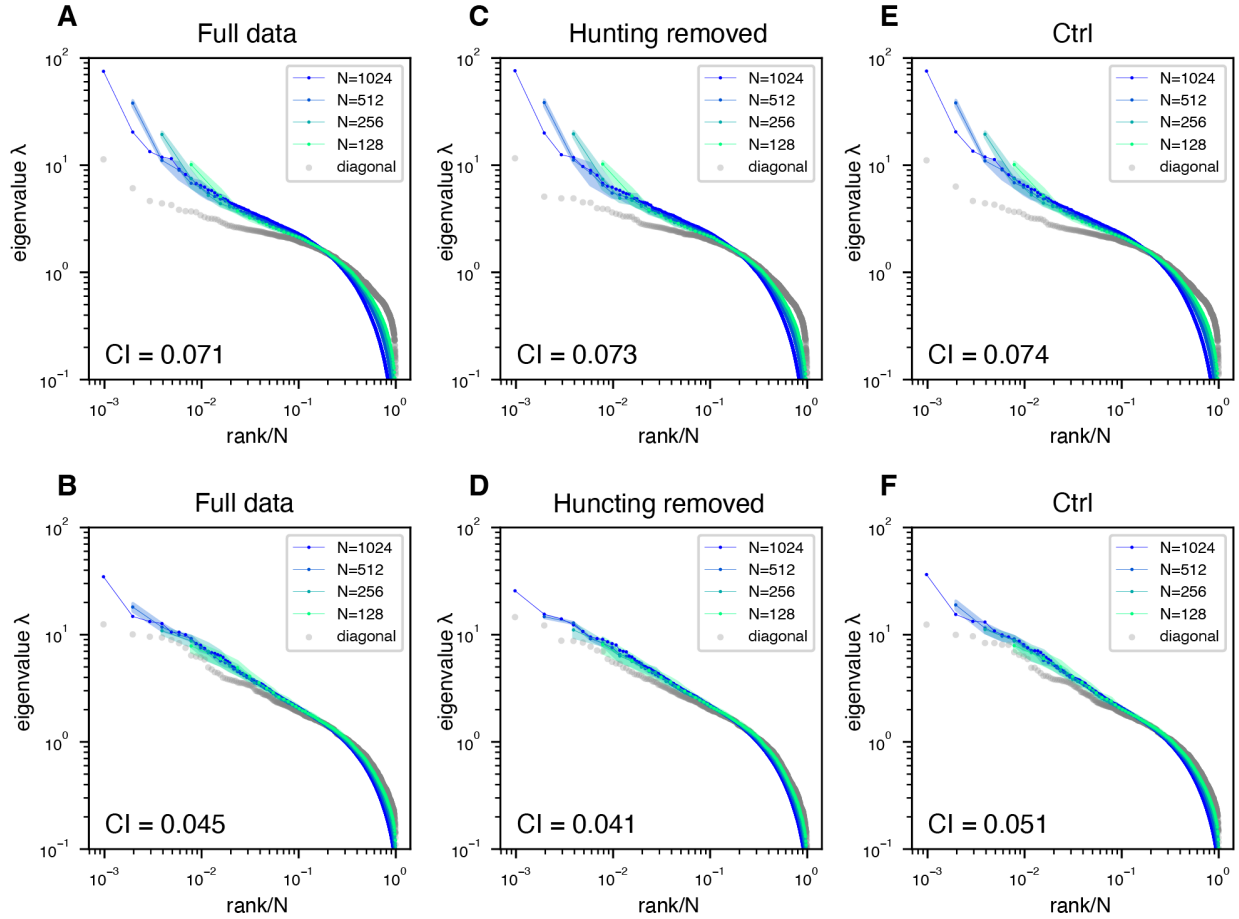

Figure S10. Removing the time segment of prey capture behavior does not obliterate the scale-invariant eigenspectra. Subsampled eigenspectra of other fish data. The first row represents fish 1 and the second row represents fish 3. **A,B.** Full data: using the entire recording time frames to calculate the covariance matrix. **C,D.** Hunting removed: data obtained by removing hunting frames from the full data (Methods). **E,F.** Ctrl: similar to **A** or **B**, but we randomly remove the same number of time frames as in **C** or **D** that are *not* from putative hunting frames.

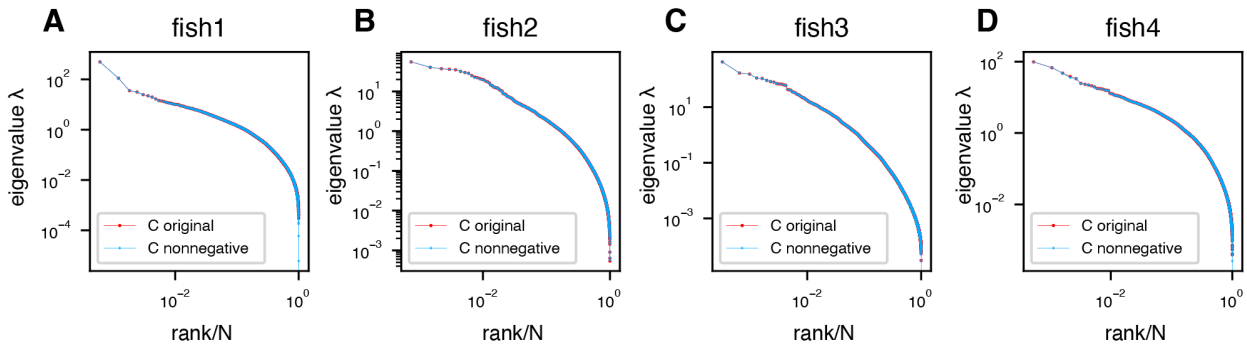

Figure S11. Negative covariances do not affect the eigenspectrum of the zebrafish data. Red: eigenspectrum of original data covariance matrix. Blue: eigenspectrum of the covariance matrix with negative entries replaced by zeros.